2016

Laser Filament Interaction with Aerosols and Clouds

Cheonha Jeon
University of Central Florida

LASER FILAMENT INTERACTION WITH AEROSOLS AND CLOUDS

by

CHEONHA JEON
B.S. University of Rochester, 2009
M.S. Yale University, 2010

A dissertation submitted in partial fulfillment of the requirements
for the degree of Doctor of Philosophy
in the College of Optics and Photonics
at the University of Central Florida
Orlando, Florida

Spring Term
2016

Major Professor: Martin Richardson

ABSTRACT

A high powered ultrashort laser pulse can propagate as a diffraction-free self-channeled structure called a filament, created by a combination of nonlinear processes. With its ability to convey extremely high intensity beams to distant targets, many applications such as remote sensing, cloud seeding, and discharge guiding are potentially possible. However, one of the main challenges of outdoor field applications is the laser propagation through the atmosphere where pressure fluctuations and concentrations of aerosols may be present. The rationale behind the work presented in this dissertation is to evaluate the robustness of the filamentation, measure the interaction losses as well as understanding the modifications to (i) filament length (ii) supercontinuum generation, and (iii) the beam profile along propagation through perturbed media.

Detailed studies of the interaction of a single filament with a single water droplet are presented. In addition, preliminary results on filament propagation through a cloud of aerosols are discussed. The effect of pressure on the beam profile along propagation and on the supercontinuum generated by the filament is studied. This document provides valuable insight into the complex nonlinear processes affecting the formation, propagation and post propagation of filaments under adverse atmospheric conditions.

For God, for Country, for Family

TABLE OF CONTENTS

LIST OF FIGURES

LIST OF TABLES

LIST OF ACRONYMS/ABBREVIATIONS

AOI	Angle of incidence
AOPDF	Acousto-optic programmable dispersive filter
CCD	Charge-coupled device
CLaPTAM	Chamber for laser propagation through aerosol medium
CPA	Chirped-pulse amplification
CW	Continuous wave
FIBS	Filament induced breakdown spectroscopy
FWHM	Full width half max
HOKE	Higher-order Kerr effect
HTP	High temperature plasmas
ICCD	Intensified charge coupled device
LIBS	Laser induced breakdown spectroscopy
LIDAR	Light detection and ranging
LPL	Laser plasma laboratory
LTE	Local thermal equilibrium
LTP	Low temperature plasmas
MPA	Multi photon absorption
MPI	Multiphoton ionization
MTFL	Multi-terawatt femtosecond laser
NA	Numerical aperture
NLSE	Nonlinear Schrödinger equation
SLR	Single-lens reflex
SPM	Self-phase modulation
VHMMS	Virtual hyperbolic metamaterials

INTRODUCTION

Laser filaments possess the unique property of propagating as a diffraction-free self-channeled structure for kilometer range distances [1]. This characteristic has opened the door to many potential applications with the need of delivering high intensities to remote distances. However, as the beam travels in the atmosphere over long distances, its interaction with aerosols (such as in clouds and fogs), dust particles and atmospheric turbulence are inevitable. One of the main objectives of this dissertation is to investigate the effect of these interactions on the filament propagation under adverse atmospheric conditions.

Near-infrared light detection and ranging (LIDAR) at an altitude of 4 km with the filament used as a light source was demonstrated [2]. This study well demonstrates the potential of filaments for long-distance propagation applications. However, the atmospheric optical limits need to be addressed. For filament applications like LIDAR, where the filament needs to propagate to high altitudes, a change in the pressure is inevitable. The nonlinear processes involved in filament formation are affected by the pressure of the propagating medium. Drastic changes in the supercontinuum generated by the filament, due to pressure variance, could limit the detection range. Reduced nonlinear effect on the filamentation process at lower pressures will eventually not have enough influence on the beam to counter the diffraction of propagating beam. This will result in an increase in the beam size, leading to decrease in beam intensity.

Aerosols and dust particles in the atmosphere could limit the optical propagation of laser beams. As the beam interacts with an aerosol, it may be absorbed, refracted, scattered or

reflected depending on the properties of the interacting aerosol. For applications such as discharge guiding and cloud seeding, it is important to understand how the filament propagates through an aerosol medium. In addition to this, it is also necessary to understand how the filament itself affects this medium.

The challenges in atmospheric propagation of filaments in realistic conditions are addressed in this study, answering the following questions:

1. How do the characteristics of a filament change as it interacts with an aerosol?
2. How much of energy is lost during this filament-aerosol interaction?
3. What mechanisms are responsible for the energy loss?
4. What happens to the aerosol as it interacts with a filament?
5. How do the characteristics of a filament change with the pressure of the medium?

An overview of the basic theory of laser-matter interaction, characteristics of laser filaments, and filament applications are provided in Chapter1. The experimental facilities that are used for the filament propagation studies are exposed in Chapter 2. Chapter 3 discusses the fundamental studies of filament-aerosol interaction, characterizing the filament propagation before and after it interacts with an aerosol. In addition, the techniques used to measure the energy dissipation of the filament as well as simulations and experimental data on the single filament-single water droplet interaction are mentioned. Changes in the characteristics of the filament at different pressures are presented in Chapter 4. Beam profile and spectral

measurements of the filament propagating in different pressures are presented. The conclusion to the findings of this work is described in Chapter 5.

1 FILAMENTATION

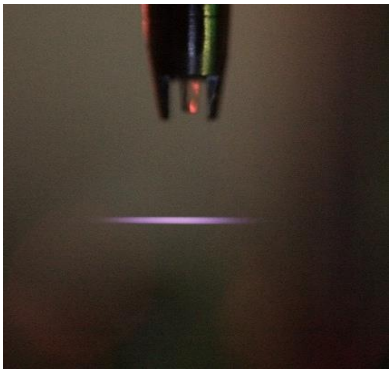

Figure 1.1: Picture of a laser filament taken with a digital SLR camera

Self-trapping of a laser beam was first proposed in 1964 by Chiao *et al.* [3]. It has now been two decades since Braun *et al.* discovered filamentation in air in 1995 [4]. Since then, there has been a rapid progress in research in this field [5-8].

1.1 Filamentation Theory

A laser filament is a diffraction-free propagating beam that is generated by high-power ultrashort lasers. A laser pulse with a peak power greater than a critical value (~ 10 GW in air at 800 nm [9]) propagating in air will experience self-focusing due to the optical Kerr effect and focuses to a high intensity spot. The focused beam is sufficiently intense to generate a weak plasma in the air. The presence of the free electrons decreases the effective refractive index locally, causing the propagating beam to diverge. The balance between the optical Kerr self-focusing and plasma defocusing results in a diffraction-free self-sustaining plasma structure.

These filaments, with a high optical intensity of ~5 x 10^{13} W/cm^2 [5] in the core can propagate over long distances.

1.1.1 Kerr Self-Focusing

As a laser beam with high powers propagates through a medium, the refractive index of the medium is altered by the Kerr effect. This change in refractive index is given by [10]:

$$n(r,t) = n_o + n_2|E(r,t)|^2 = n_o + n_2 I(r,t) \qquad (1\text{-}1)$$

where n_o is the linear component of the refractive index and n_2 is the nonlinear refractive index (cm^2/W) and $I(r,t)$ is the intensity distribution (W/cm^2) of the pulse with respect to its radial (r) and temporal (t) components.

Due to Gaussian beam profile, intensity is higher in the center of the beam than the edge of the beam. Since the nonlinear refractive index is intensity dependent, the Gaussian shape pulse will experience different refractive indices across its transverse profile, resulting in Kerr self-focusing.

The nonlinear refractive index, n_2, mentioned above is also a part of the Kerr effect and has the following equation [5, 11, 12]:

$$n_2 = \frac{3\chi^{(3)}}{4\epsilon_o c n_o^2} \qquad (1\text{-}2)$$

where $\chi^{(3)}$ is the third order susceptibility of the medium (esu), ϵ_o is the permittivity of free space (F/m), c is the speed of light (m/s) in vacuum and n_o is the linear refractive index of the medium.

The nonlinear refractive index of air (1atm, 300 K) is 3.01 x $10^{-19}$$cm^2$/W [13]. Assuming a Gaussian pulse, the central part of the beam experiences a higher refractive index than that of the low intensity edge. This is equivalent to a plane wave propagating through a convex lens where the central part of the propagating wave travels through the thicker part of the lens while the edge of the propagating wave travels through the thinner part of the lens (Figure 1.2 a). The beam then propagates through the nonlinear refractive index and self-focuses, resulting in higher intensity of the laser leading to even higher refractive index. This process continues until the whole beam collapses (Figure 1.2 b). However, this nonlinear process cannot be achieved if the power of the laser is not high enough to induced the Kerr self-focusing. This threshold power is called the critical power and is discussed in the following section.

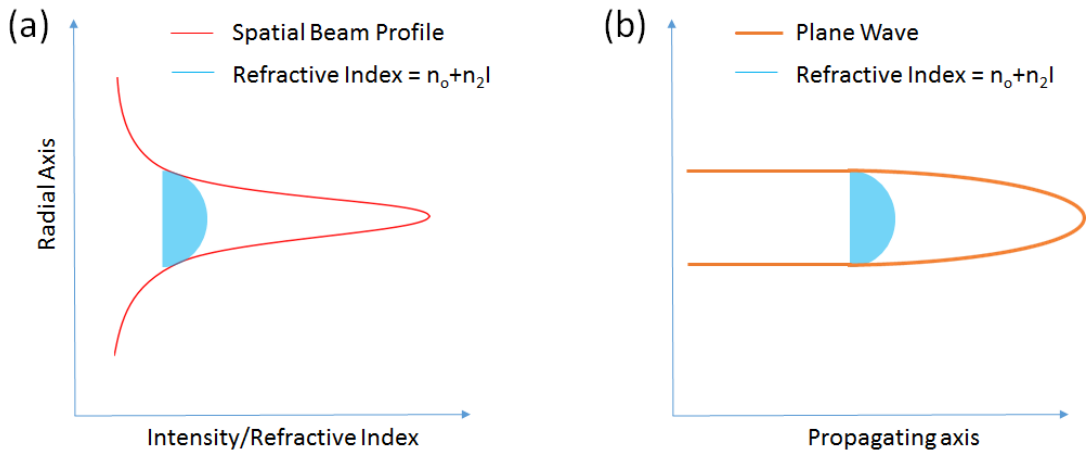

Figure 1.2: (a) Spatial distribution of the nonlinear refractive index with respect to the spatial distribution of the beam intensity for the initial beam above the critical power. (b) The self-collapse of the beam as it propagates through nonlinear medium.

1.1.2 Critical Power

For an ultrafast laser pulse propagating with its power above the critical power, the nonlinear refractive index will focus the laser pulse and cause it to collapse to a Townes profile [14, 15]. Above this threshold value, self-focusing overcomes diffraction, causing the collapse of the pulse. It can be calculated as follows [16, 17, 18]:

$$P_{cr} = \frac{\alpha \lambda_0^2}{4\pi n_0 n_2} \qquad (1\text{-}3)$$

where α is a constant depending on the spatial profile of the beam (3.72 for the Townes beam and 3.77 for Gaussian beam [5]), λ_o is the center wavelength (m) of the pulse, n_0 and n_2 are the linear and nonlinear refractive index, respectively.

Marburger [16] proposed an expression for the collapse point z_c of a continuous (CW) Gaussian beam that exceeds the critical power:

$$z_c = \frac{0.184 w_0^2 k_0}{\sqrt{\left(\left(\frac{P}{P_{cr}}\right)^{\frac{1}{2}} - 0.853\right)^2 - 0.0219}} \qquad (1\text{-}4)$$

where P is the input power (W) of the CW laser, P_{cr} is the critical power (W) of the medium, k_0 is the wavenumber (m^{-1}) of the electromagnetic wave and w_0 the Gaussian beam waist. If a lens is introduced to assist the focusing conditions, the collapse point z_f is defined as [19]:

$$\frac{1}{z_f} = \frac{1}{f} + \frac{1}{Z_c} \qquad (1\text{-}5)$$

where *f* is the focal length (m) of the lens.

1.1.3 Multi-Photon Ionization (MPI)

The ionization of an atom occurs when the interacting electromagnetic wave has a photon energy larger or equal to the ionization potential of the atom, ion or molecule [20]. In the case where the photon energy is lower than the ionization potential, ionization process can still occur if the intensity of the laser is high enough. The electrons can simultaneously absorb more than one photon to overcome the ionization potential as shown in Figure 1.3. This phenomenon is called multiphoton ionization [21, 22]. The rate of the multi photon ionization is proportional to I^K where I is the laser intensity and K is the total number of photons absorbed [23]. The ionization potential for oxygen molecules is 12 eV [24]. Therefore, it requires 8 photons of 800 nm beam ($\hbar\omega \approx 1.55$ eV) to overcome the ionization potential of oxygen and the rate of multi photon ionization will be proportional to I^8.

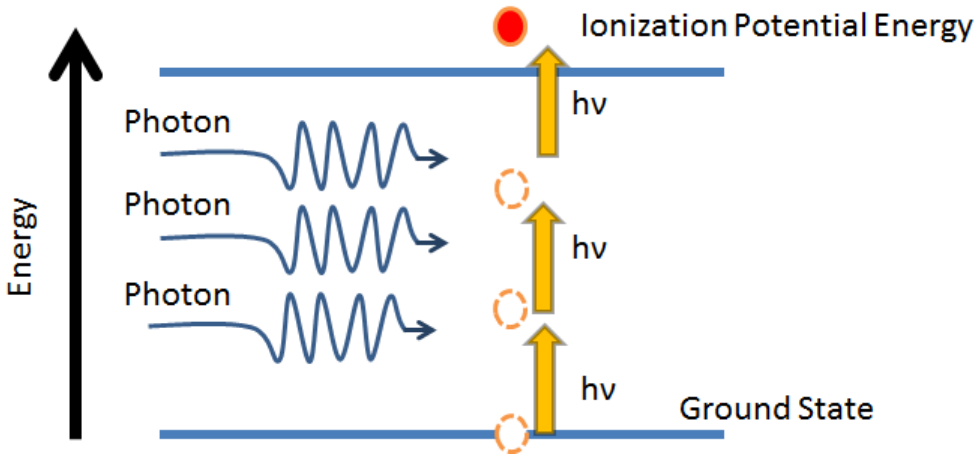

Figure 1.3: Multiphoton Ionization

1.1.4 Tunneling Ionization

Tunneling ionization occurs when the external electric field generated by the high intensity laser pulse perturbs the Coulomb potential of the nucleus, enabling an electron to escape [25, 26]. The deformation caused by the strong electric field (Figure 1.4) decreases the width of the potential barrier, increasing the probability of tunneling ionization. Tunneling ionization can take place when the period of wavelength of the laser is longer than the time the electron takes to travel through the distorted barrier. This indicates that the tunneling ionization is more likely to occur for longer laser wavelengths.

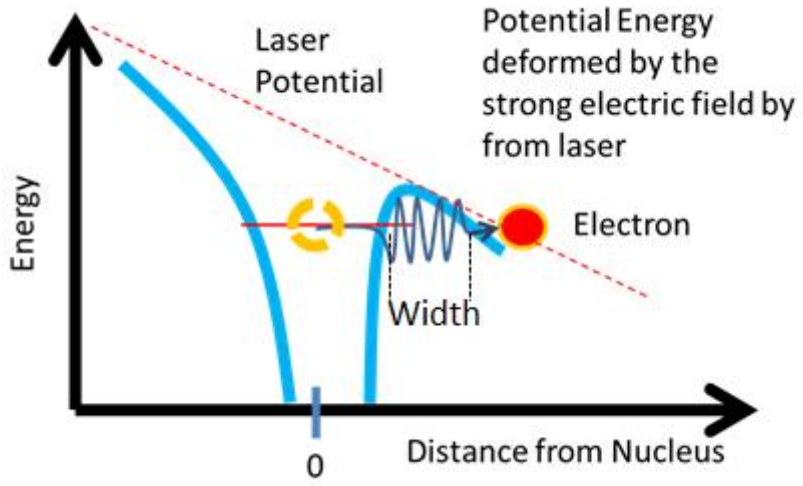

Figure 1.4: Tunneling Ionization

1.1.5 Keldysh Parameter

A theory of ionization by laser fields was described by Keldysh in 1965 [27, 28]. As a high intensity laser pulse interacts with matter, the high electrical field from the laser interacts with the electrons, inducing tunneling or multiphoton ionization. The adiabaticity parameter (Keldysh parameter) and is expressed as [27, 28]:

$$\gamma = \frac{\omega}{\omega_T} = \frac{\omega\sqrt{2m_e E_I}}{eE} \qquad (1\text{-}6)$$

where ω is the laser frequency (Hz), ω_T is the frequency (Hz) of the electron tunneling through the potential barrier, E_I is the ionization potential (eV), E is the electric field intensity (V/cm), and m_e and e are the effective mass (kg) and charge (C) of the electrons, respectively. The tunneling ionization process will dominate the ionization process when $\gamma << 1$ and multiphoton process will dominate if $\gamma >> 1$.

The ionization potential for oxygen and nitrogen molecules is 12 eV and 15.6 eV respectively [29, 24]. Therefore, for a laser (800 nm)-induced filament in air, the Keldysh parameter is calculated to be ~ 1.8.

1.1.6 Plasma Defocusing

Based on Drude model, the contribution n_c from the electron density of the plasma to the refractive index of the local medium can be written as [30]:

$$n_c \approx -\frac{\rho(r,t)}{2\rho_c} \qquad (1\text{-}7)$$

where $\rho(r,t)$ is the instantaneous and local density of free electrons and $\rho_c \equiv \epsilon_o m_e \omega_o^2/e^2$ is the critical plasma density [ϵ_o is permittivity (F/m) in vacuum, ω_o is the laser frequency (Hz) and m_e and e are electron mass (kg) and charge (C)]. This local decrease in refractive index due to plasma generation would act like a negative lens resulting in the divergence of the laser beam [18]. The plasma-induced divergence and diffraction mechanisms will then overcome the self-focusing mechanism, inducing divergence of the pulse. As long as the beam has enough power, above the critical power, the self-focusing term dominates again over the defocusing mechanisms and this oscillation of self-focusing and defocusing continues until the filament stabilizes. The stable filament consists of an intense core with a clamped intensity (~ 5 x 10^{13} W/cm^2) and an energy reservoir as shown in Figure 1.5. The filament, however, will lose its power due to multi-photon absorption and will not have enough power to overcome the diffraction, leading to divergence of the beam therefore termination of filamentation.

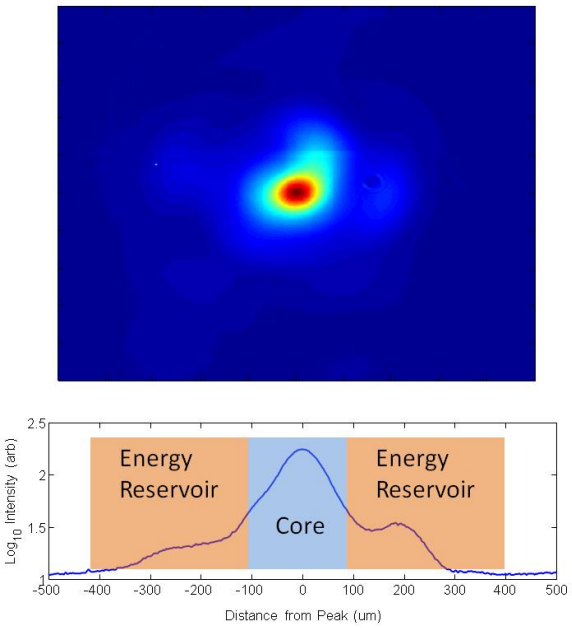

Figure 1.5: Beam profile of the filament generated with Ti:sapphire laser (2.2 mJ, 800 nm, 50 fs) using 1.2 m focusing lens.

1.1.7 Higher-Order Kerr Effect (HOKE)

There is a controversy between the plasma defocusing and self-defocusing caused by higher-order Kerr effect (HOKE) [11, 31-33]. The measured coefficients of the higher order nonlinear refractive index of nitrogen, oxygen and air have shown that the n_4 and n_6 terms are negative, leading to a Kerr self-defocusing effect [34]. However, for this dissertation, the filaments are described as a dynamic balance between Kerr self-focusing and plasma defocusing. The basic theory, characteristics and applications of filaments generated from femtosecond pulses at 800 nm will be in the following section.

1.1.8 Dynamic Spatial Replenishment Model

The dynamic spatial replenishment model was proposed by Mlejnek *et al.* to explain filamentation [35]. This model considers the temporal pulse shape to consist of a series of thin time slices. Assuming a Gaussian temporal profile of the beam, the central time slice has the highest intensity, reaching self-focusing first. The focused time slice ionizes the air and is defocused. The slices that are temporally earlier than the central time slice go through the same process at farther distances as long as their power is above the critical power. However, the trailing edge of the pulse is defocused by the plasma generated by the central and earlier slices. This focusing-defocusing process repeats as long as the time slices have sufficient power, above the critical power, to counter the diffraction with Kerr self-focusing. The pulse loses its power to multi photon ionization (MPI) as it propagates, and diverges eventually.

1.1.9 Nonlinear Schrödinger Equation

Filament propagation can be numerically described by the nonlinear Schrödinger equation (NLSE):

$$\frac{\partial \varepsilon}{\partial z} = \frac{i}{2k}\left(\frac{\partial^2}{\partial x^2} + \frac{\partial^2}{\partial y^2}\right)\varepsilon + ik_0 n_2 |\varepsilon|^2 \varepsilon - \frac{ik_0}{2n_0}\frac{\rho}{\rho_c}\varepsilon \qquad (1\text{-}8)$$

where k and k_0 are the wavenumber of the electromagnetic wave in the medium and vacuum respectively, n_2 and n_0 are nonlinear and linear refractive index of the medium respectively , ρ is the free electron density and ρ_c is the critical plasma density. $|\varepsilon|^2$ is defined to be the intensity that is expressed as $1/2 n_0 \epsilon_0 c|E|^2$ where ϵ_0, c, and E are the permittivity of free space, speed of

light, and electric field of the electromagnetic wave respectively. The right hand side of the equation represents the diffraction term, Kerr self-focusing and plasma defocusing respectively.

More physical effects such as group velocity dispersion (k''), molecular Raman-Kerr effect, plasma absorption, and MPI losses have been added to the NLSE equation (1-8) for this dissertation.

$$\frac{\partial \varepsilon}{\partial z} = \frac{i}{2k}\left(\frac{\partial^2}{\partial x^2} + \frac{\partial^2}{\partial y^2}\right)\varepsilon - \frac{ik''}{2}\frac{\partial^2 \varepsilon}{\partial y^2} + N_{kerr} + N_{plasma} + N_{MPA} \quad (1\text{-}9)$$

$$N_{kerr} = ik_0 n_2(1-\alpha)|\varepsilon|^2\varepsilon + ik_0 n_2 \alpha\left[\int_{-\infty}^{t} R(t-t')|\varepsilon(t')|^2 dt'\right]\varepsilon \quad (1\text{-}10)$$

$$N_{plasma} = -\frac{\sigma}{2}(1 + i\omega_0\tau_c)\rho\varepsilon \quad (1\text{-}11)$$

$$N_{MPA} = -\frac{K\hbar\omega_0\rho_{nt}\sigma_K}{2}|\varepsilon|^{2K-2}\left(1 - \frac{\rho}{\rho_{nt}}\right)\varepsilon \quad (1\text{-}12)$$

$$R(t) = \frac{\Gamma^2 - \omega_R^2}{\omega_R^2}\, exp(-\Gamma t)\, sin\omega_R t \quad (1\text{-}13)$$

In the optical Kerr term (1-10), α denotes the fractional distribution of the Kerr self-focusing effect to an instantaneous electron response and a delayed molecular Raman scattering. In the plasma term (1-11), σ is the cross section for inverse Bremsstrahlung, ω_0 is the laser frequency, and τ_c is electron collision time where the inverse Bremsstrahlung is a further acceleration of the electrons due to the electric filed of the remaining part of the pulse. In the multi-photon absorption (MPA) term (1-12), $\hbar$ is the reduced Planck's constant (1.055 x 10^{-34} Js), ρ_{nt} is the density of neutrals in the medium, and σ_K is the K-photon ionization cross section. For the molecular response of the medium (1-13), Γ^{-1} denotes the molecular response time and ω_R

denotes the molecular rotational frequency. The values for each parameter used in this simulation in this thesis are listed in Table 1.

Table 1: List of parameters for the simulation at 800 nm

Parameters	Air
n_2 ($\times 10^{-19}$ cm^2/W)	2.9
k'' (fs^2/cm)	0.2005
σ_K ($s^{-1}cm^{2K}W^{-K}$)	2.81 x 10^{-96}
U_i (eV)	12.063
K (λ = 800 nm, $\hbar\omega \approx$ 1.55 eV)	8
Γ^{-1}(fs)	70
ω_R ($\times 10^{12}$ s^{-1})	16

1.2 Filament Properties

In this section, the basic characteristics of the filament are discussed including its plasma density, energy distribution, length, and spectrum.

1.2.1 Filament Plasma Density

The high intensity of the filament at its core ionizes the medium in which it propagates. Several studies have measured the density of the free electrons generated by the high intensity core of the filament [36-43]. The reported electron density varies from 10^{12} cm^{-3} [38] to $10^{18}cm^{-3}$ [39].

This wide range of electron density may be caused by the initial pulse condition (pulse width and energy) as well as focusing conditions used to induce filamentation [36].

1.2.2 Intensity Clamping

As discussed above, filamentation is the result of the dynamic balance between self-focusing mechanism in a nonlinear medium and plasma. The rate of the multi photon ionization, being the dominant ionization process, is proportional to I^K where I is the laser intensity and K is the total number of photons absorbed to overcome the ionization potential [23]. As the intensity of the filament increases by self-focusing, the rate of the multi-photon ionization (MPI) increases, resulting in a fast increase in electron density that will defocus the filament. Therefore a limit to the filament peak intensity is set by this balance leading to a very stable intensity throughout the length of the filament [44]. The value of this clamped intensity was reported in the order of 5 x 10^{13} W/cm^2 [4, 5].

1.2.3 Spatial Distribution of Energy within a Filament

The reported filament peak intensity varies in the orders of 10^{13}W/cm^2 to 10^{14}W/cm^2 [45, 46, 47]. However, most of the input laser energy is not channeled within the core of the filament. According to Brodeur, *et al.* [45], the energy within the core of the filament does not exceed 7% of the total energy. This indicates that the rest of the total energy either is scattered by the medium or concentrated in the region surrounding it called “energy reservoir”. This energy reservoir plays a major part in filamentation since it reforms the filament even if the core of the filament is blocked [48- 51]. On the other hand, if the reservoir of the filament is blocked, the filament is no longer

generated [7, 52]. Figure 1.6 shows a study by W. Liu *et al*. on the impact of the energy reservoir on the filament propagation [48]. Both numerical and experimental data show that as the size of the pinhole blocking the energy reservoir decreases, the length of the filament decreases as well.

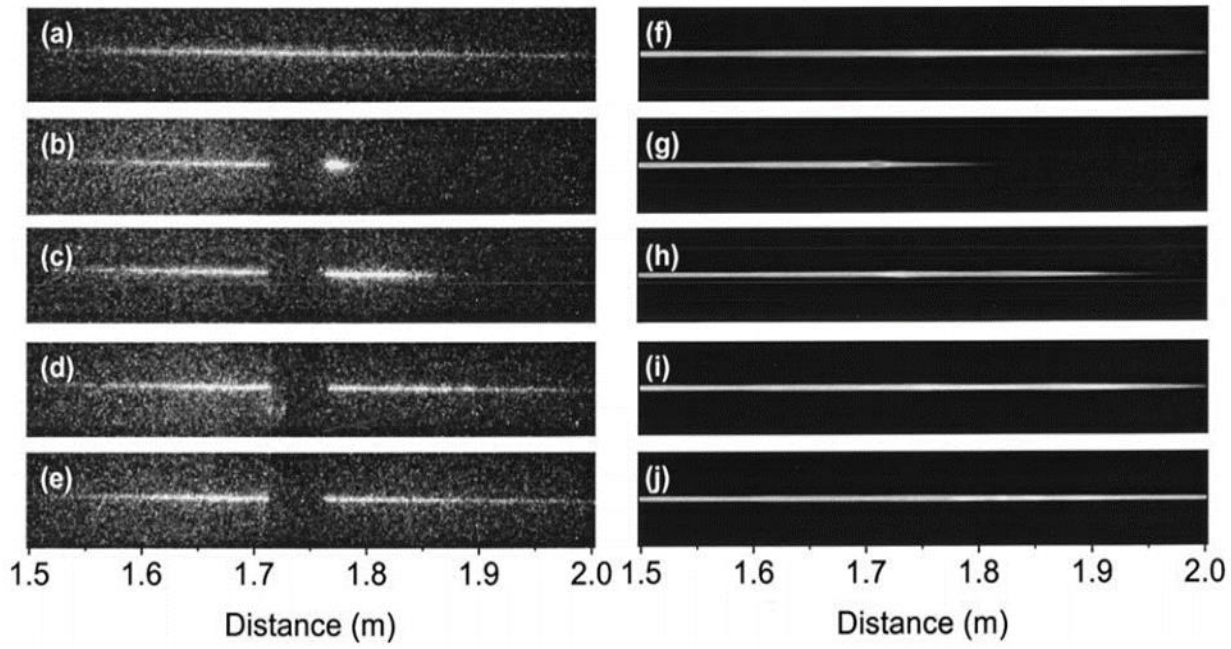

Figure 1.6: Left column, images of filament taken by an ICCD. Right column, electron density distribution from numerical simulation. (a), (f) free propagation; (b), (g) 220 μm pinhole diameter; (c), (h) 440 μm pinhole diameter; (d), (i) 1 mm pinhole diameter; (e), (j) 2 mm pinhole diameter. Source: [48]

1.2.4 Length of a Filament

The length for which the laser intensity is sufficient to ionize the propagation medium defines the general definition of the filament length. One way to characterize the length of the

filament is by taking the side image of the plasma emission from the nitrogen molecular ion (N_2^+, $B^2\sum_u^+ \rightarrow X^2\sum_g^+$) at 391 nm [36]. Figure 1.7 (a) shows an overlay of the image of the filament taken with 30 seconds exposure in a completely dark room on top of the image of the setup with 0.025 second exposure with the lights on. This image was taken with a standard digital SLR camera while Figure 1.7 (b) was taken with an ICCD with 5 μs gate width and 200 accumulations.

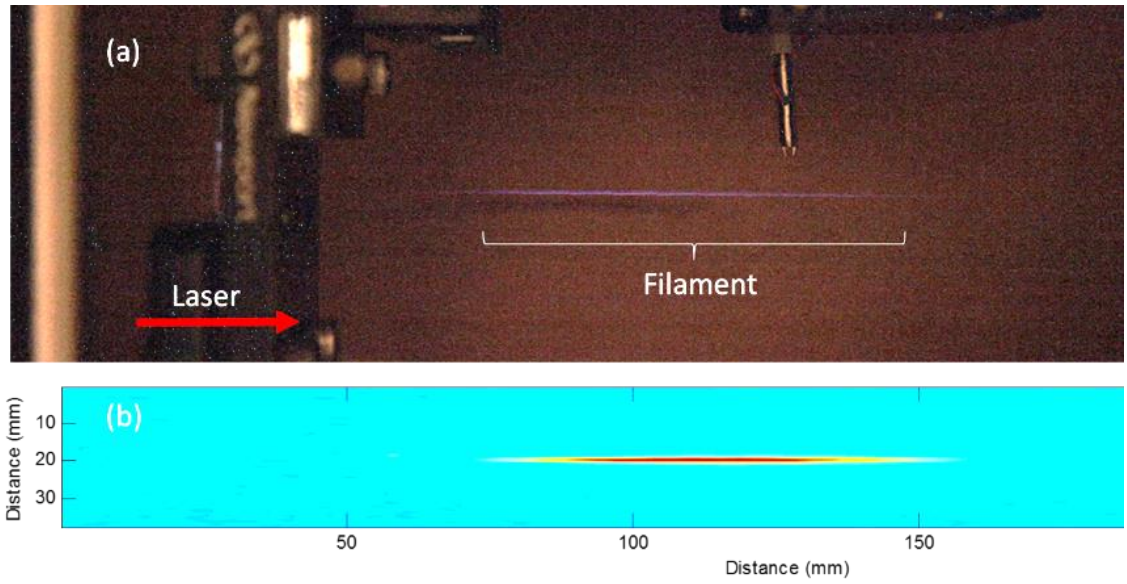

Figure 1.7: The side view images of filament taken with (a) a standard digital SLR camera, (b) an ICCD.

The lifetime of the plasma (several ns) is longer than the temporal width of the laser pulse. Applications utilizing the filament plasma channel are discussed in Section 1.3.

1.2.5 Supercontinuum

1.2.5.1 Self-Phase Modulation (SPM)

As the pulse propagates in a nonlinear medium, new frequencies are generated in the spectrum of the pulse due to the variations of the index of refraction induced by the time dependent intensity (Equation 1-1). This Self-phase modulation (SPM) the temporal aspect of the Kerr effect causes a modification of the temporal profile generating new components in the spectrum towards a supercontinuum [53- 55]. The instantaneous and local electromagnetic field of a plane wave can be described as following [7]:

$$E(z,t) = exp(i\Phi) = exp\left(i\left(\omega_o t - \frac{\omega_o n}{c} z\right)\right) \qquad (1\text{-}14)$$

where Φ is the instantaneous phase of the pulse, ω_o is the angular frequency of the laser and n is the refractive of the medium. The link between the instantaneous frequencies and the pulse intensity can be expressed as [56]:

$$\omega(t) = \frac{\partial \Phi}{\partial t} \sim \omega_o - \frac{n_2 \omega_o}{c} z \, \frac{\partial I(r,t)}{\partial t} \qquad (1\text{-}15)$$

As the pulse propagates, its rising edge generates lower frequencies while the falling edge broadens the spectrum towards the blue.

1.2.5.2 Self-Steepening

Self-steepening also contributes to the spectral broadening by changing the temporal profile of the pulse. The intensity dependent nonlinear refractive index, $n_2 I$, leads to a different

propagation speed for the different parts of the pulse. The peak of the pulse will have a slower velocity compared to the lower intensity parts. This will result in a steepening of the intensity profile, resulting in a lower frequency of the electric field, generating more blue in the spectrum.

1.2.5.3 Time Dependent Plasma Density

The ionization of the propagating medium does not only induce the divergence of the beam but it also contributes to the broadening of the spectrum. The instantaneous higher frequency generation due to the dynamics of the plasma can be added to the instantaneous frequency (Equation 1-15):

$$\omega(t) = \frac{\partial \Phi}{\partial t} \sim \omega_o - \frac{n_2 \omega_o}{c} z \frac{\partial I(r,t)}{\partial t} + \frac{\omega_o}{2 n_o \rho_c c} z \frac{\partial \rho(r,t)}{\partial t} \qquad (1\text{-}16)$$

Other than these basic mechanisms for spectral broadening, several studies have been conducted to further enhance supercontinuum generation by controlling the initial parameter [57], elliptical polarization [58], spatial chirp [59] and seed pulses [60] to the filament.

1.2.6 THz Generation

In addition to the spectral broadening into higher and lower frequencies by the nonlinear phase propagation, THz pulses are generated from the plasma channel. The radial gradient of the laser intensity generates the pondermotive force acting on the ionized electrons of the plasma leading to THz generation [61, 62, 63]. The applications using THz is explained in Section 1.3.

1.2.7 Robustness

Filamentation has gained attraction from its robust propagation and its ability to reform after interacting with microscopic obstacles. This process of self-healing [50, 64] is intrinsic to the energy reservoir of the filament where the most of the energy is embedded in. Even if the core of the filament is completely blocked by an obstacle, the filament will heal back to its original shape as long as the energy reservoir has enough energy to induce Kerr self-focusing [65, 66]. However, as it can be seen from Figure 1.6, when the pinhole size that blocks the energy reservoir decreases, the length of the filament decreases, leading to the termination of the filament [48]. This is due to the energy leakage from the diffraction of energy, caused by the pinholes, at the edge of the energy reservoir.

1.2.8 Long Propagation

The ultrashort pulse with the clamped intensity minimizes the energy loss of the propagating beam by allowing minimum amount of energy for MPA to enable the dynamic balance between Kerr self-focusing and plasma defocusing. This allows the filament to propagate for long distances as a diffraction free self-channeled structure. Long propagation of high intensity filament ($>10^{12}$ W/cm^2) has been demonstrated over kilometric distances [1, 67].

1.3 Applications of Filaments

The ability of filaments to propagate over long distances as a diffraction free self-channeled structure, has led to a wide range of applications. The propagation of high intensity

beams to remote targets and generation of white-light continuum have attracted the remote sensing community while the formation of long plasma channels has triggered new ideas for microwave and discharge guiding. This section discusses some of the most actively researched filament applications.

1.3.1 Remote Sensing

Two unique characteristics of filaments stand out for remote sensing applications. The ability of propagating as a diffraction free high intensity beam over long distances could be used as the source for LIBS while white-light emission could be used as an ideal source for absorption LIDAR [58, 68-71].

1.3.1.1 Filament Induced Breakdown Spectroscopy (FIBS)

Laser induced breakdown spectroscopy (LIBS) uses the intense laser pulse on a target surface to generate plasma. This plasma contains the ablated mass in the form of positive and negative ions. The excited particles then relax to their ground state resulting in photon emissions that can be used as atomic finger prints to identify elemental composition of the target. The high intensity (~$5x10^{13}$ W/cm^2) self-channeled beam can ablate the surface of far distance targets that might not be reached by nanosecond-lasers. Nanosecond-lasers have to overcome diffraction as well as inverse Bremsstrahlung for remote sensing using LIBS. However, femtosecond filaments can propagate over long distances and avoid major energy loss in plasma-laser interaction. In addition, femto-LIBS have lower plasma temperature than that of the nano-LIBS, resulting in negligible nitrogen and oxygen emission from excited ambient air [72, 73, 74]. Standoff FIBS on

copper and steel at a distance of 90 m and on aluminum at a distance of 180 m have been demonstrated [73, 75, 76].

1.3.1.2 Light Detection and Ranging (LIDAR)

Supercontinuum generation of a filament is an ideal white light source for absorption LIDAR to detect pollutants in atmosphere [77]. Humidity and temperature of the atmosphere can be calculated from the magnitude of water vapor lines (humidity dependent) and the width of the oxygen lines (temperature dependent) [78]. Compared to the conventional LIDAR, which requires wavelength scanning, the filament based LIDAR has a broadband source that enables a single-shot acquisition for the entire spectrum range of ~ 220 nm to 4.5 μm [79, 80]. In addition to the broad spectral range, a strong backward emission of the spectrum was also observed [81], which is extremely advantageous for absorption LIDAR. The absorption spectrum of the ro-vibrational molecular oxygen and ro-vibrational H_2O were measured using filament based LIDAR technique [77, 82]. Near-infrared LIDAR at an altitude of 4 km [2] and white-light LIDAR at 100TW power level [83] were demonstrated with a filament used as a light source.

1.3.1.3 THz Generation and Sensing

Filamentaion can generate partially directional THz spectrum ranging from 1 to 20 THz [84-86]. This broad THz range of the spectrum is where the fingerprint of organic compounds can be detected. Therefore filament in air can be used to detect and characterize chemical compounds such as contraband drugs and explosives [87-89].

1.3.2 Guiding

The self-channeled plasma structure of the filament can be used as a virtual waveguide to guide microwaves or discharges. In this section, proposed guiding application of the self-channeled plasma structure of the filament will be discussed.

1.3.2.1 Guiding Microwaves

The self-channeled plasma structure can be used to guide microwaves [90- 92]. Using the property of a waveguide, multiple plasma channels can form a plane that can reflect the frequencies below the plasma frequency. Therefore microwave radiations with frequencies below 30 GHz, can be guided through the laser filament based waveguide in a similar way of light travelling through an optical fiber. Another proposed idea of microwave guiding is virtual hyperbolic metamaterials (VHMMs). Plasma channels from the filament can be engineered to form a compact periodic structure that can manipulate radar signals [93]. The proposed design of the VHMMs show that they are suitable for collimation and redirection of microwave beams. The challenge is generating the desired structure of multiple filaments as well as maintaining the plasma channel spatially and temporally.

1.3.2.2 Guiding Discharges

The plasma density of a free propagating filament is ~ 4.5 x 10^{14} cm^{-3} [36] while the required free electron to initiate lightning in the atmosphere is ~ 5 x 10^{11} cm^{-3} [94]. Several research groups have worked with filaments to play the role of a bridge between two highly

charged electrodes [95, 96]. In a large scale, the filament could be used to build an apparatus to safely guide lightning from cloud to earth in a pre-existing lightning condition [97, 98]. One of the main challenges to overcome in the cloud to earth lightening guiding is to generate and maintain sufficient length of plasma channel.

1.3.3 Climate Control

Several studies have been conducted to understand the impact of filaments on aerosols. These include studies on water condensation [99, 100], air-flow motion [101], aerosol formation [102], aerosol explosion [103, 104], and further leading to climate engineering [105]. The aerosol interaction with the filament creates turbulence [101] and different particle sizes [103, 104] that may play a role of cloud seeding and even generate snow [106, 107]. There are sufficient evidences that lead to laser-induced condensation/precipitation. However, the fundamental mechanisms behind it are not well understood.

1.3.3.1 Cloud Seeding

Several groups have observed filament-induced water condensation that could be used for cloud seeding [108-110]. The proposed theory behind this phenomenon is induced binary H_2O-HNO_3 nucleation due to the photo-oxidative chemistry of nitrogen with water molecules. Ju *et al*. have performed large-scale water condensation by laser filaments and found the evidence of HNO_3 from laser-assisted condensation [111].

1.3.3.2 Snow Generation

In a similar way to cloud seeding, filament-induced snow formation has also been demonstrated [111, 106]. Ju *et al.* have discovered that the snow formation was only visible for shorter external focusing conditions (f = 20 and 30 cm), while only water condensation was observed for longer focusing conditions (f = 50 and 80 cm) [112]. Leisner *et al*. have conducted an experiment in a cloud simulation chamber with a volume of 84.5 m^3 [113]. They have discovered that the laser interaction with ice clouds increases the concentration of ice particles by factor of 100 from the initial concentration. In addition to this, the newly detected ice particles grew in size to few tens of micrometers. The effect was only observed when the temperature was below -37 ^oC, the relative humidity is above unity with respect to ice, and when the preexisting ice particles are present.

2 EXPERIMENTAL FACILITIES

The study of laser filamentation and its propagation under adverse atmospheric conditions requires the control of the laser conditions as well as the propagation medium. In order to conduct such a controlled study on the mutual influence of the filament and its environment on one another, a high power ultrafast laser and a controllable atmospheric chamber were used.

This chapter provides an overview of the laser source used for filament generation as well as the full design and characteristics of the atmospheric chamber and its suite of diagnostics.

2.1 Multi-Terawatt Femtosecond Laser

The Multi-Terawatt Femtosecond Laser (MTFL) developed at the Laser Plasma Laboratory (LPL) uses Ti:sapphire crystals as gain medium with the chirped pulse amplification (CPA) method to amplify the energy of the 50 fs pulses [114] up to 230 mJ at 10 Hz . This system begins with a CW 532 nm laser (Spectra-Physics Millenia V) that pumps an Ti:sapphire-based oscillator (Spectra-Physics Tsunami) as shown in Figure 2.1. The oscillator is passively mode-locked by Kerr-lens mode-locking while an acousto-optic modulator ensures mode-locking at laser start-up. The oscillator then outputs 35 fs laser pulses at a rate of 73 MHz with a spectrum centered at 800 nm.

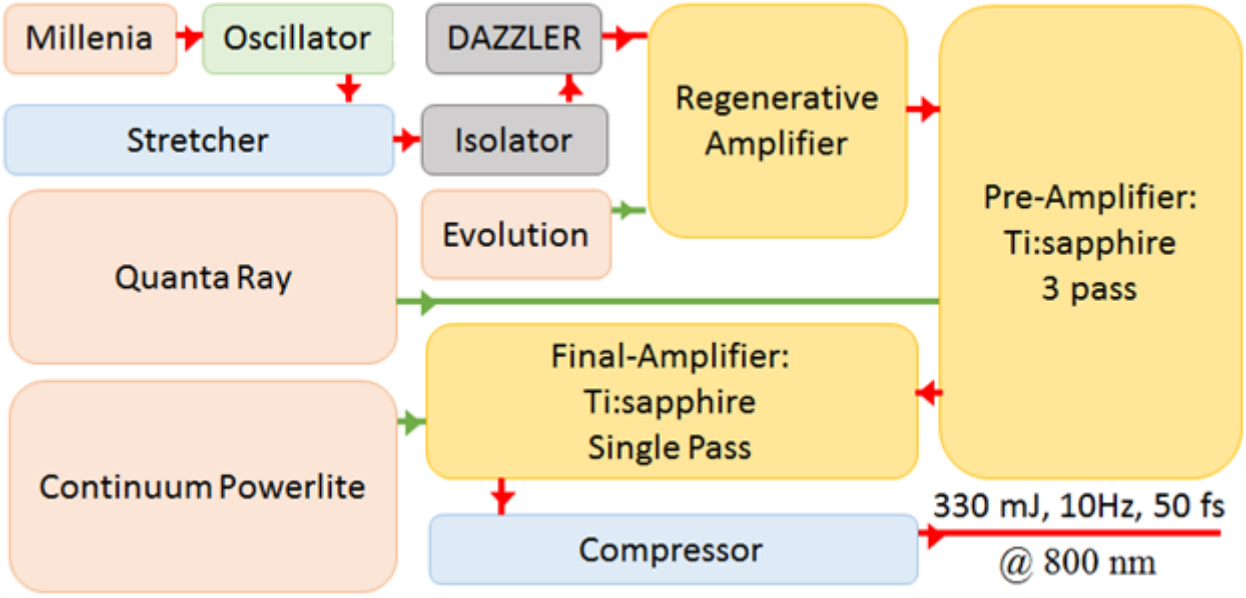

Figure 2.1: Schematics of MTFL

The pulse train from the oscillator is temporally stretched to ~450 ps using a Martinez grating stretcher to reduce the pulse power for the amplification process. The stretched pulse then passes through an acousto-optic programmable dispersive filter (AOPDF) (Fastlite, DAZZLER) which modulates the amplitude of the laser pulses in the frequency domain. After passing through the DAZZLER and a Faraday isolator to stop any back reflections, the modified pulse train is used as a seed for a regenerative amplifier. The regenerative amplifier uses Ti:sapphire as a gain medium and is pumped by a 1kHz 20W laser pulsed at 1 kHz and centered at 527 nm (Spectra-Physics Evolution-30). The Z-shaped cavity with in the regenerative amplifier includes two Pockels cells before the two high reflecting cavity mirrors. The Pockels cells allow the seed pulse to enter and exit the cavity after ~30 roundtrips resulting in 1.3 mJ of

output energy. After the regenerative amplifier, the pulse is sent through a pulse picker to reduce the repetition rate to 10 Hz and then is preamplified in a 3-pass bowtie-design Ti:sapphire amplifier. The pump of the amplifier delivers pulses at 10Hz with 750 mJ centered at 520 nm (Spectra-Physics Quanta-ray Pro290) delivered to both sides of the Ti:sapphire amplifier crystal. The output beam from 3 passes in the pre-amplifier is 130 mJ. The amplified beam experiences a final amplification in a Ti:sapphire crystal pumped by 2J pulses centered at 532 nm (Continuum Powerlite DLS). After a single pass from this final amplifier, the pulses (350 mJ) are then sent through a Tracey grating compressor to compress the pulses to ~50 fs. The system delivers ~ 50 fs pulses with 230 mJ energy at 10Hz.

2.2 Chamber for Laser Propagation Through Aerosol Medium (CLaPTAM)

As filaments propagate, they encounter pressure and temperature changes due to the change in altitudes or different landscapes. Figure 2.2 (a) shows the temperature and pressure of earth's atmosphere for altitudes from 0 to 120 km above sea-level. The clouds are spread throughout the earth atmosphere; however, most are present up to 5.5 km above sea level. The temperature and the pressure at this altitude are -20 ^{O}C and 0.5 atm respectively. To simulate the propagation of laser filament in such conditions (from ground to ~ 5.5 km above sea level), the Chamber for Laser Propagation Through Aerosol Medium (CLaPTAM) was built.

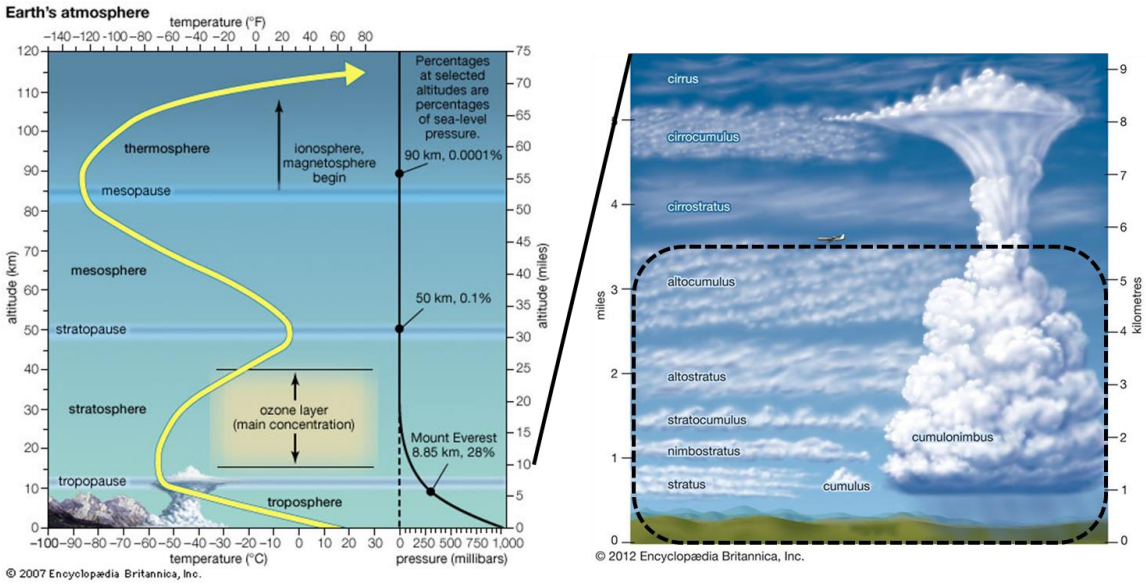

Figure 2.2: Earth's atmosphere (Source: Encyclopedia Britannica, Inc.[149])

2.2.1 Schematics of CLaPTAM

The customized chamber (built by A&N Corporation) is composed of three identical segments that can be used alone as 70 inches (1.78 m) of propagation or they can be joined together to give a maximum propagation length of 210 inches (5.33 m). The outer diameter of the chamber is 20 inches (50 cm) as shown in Figure 2.3. Each of the individual chambers has total of 10 viewing windows (5 windows on each side) with 4 inches (100 cm) of clear aperture. The chamber also has 10 ports (QF 40-150-SF) per individual segments for connection purposes. The 10 ports are used for, but not limited to:

1. Pump connection
2. Condensing unit inlet/outlet

3. Aerosol generator
4. Thermometer
5. Pressure Gauge
6. Humidity sensor
7. Fan
8. Power
9. Cleaning/drying pipeline
10. USB/trigger cable

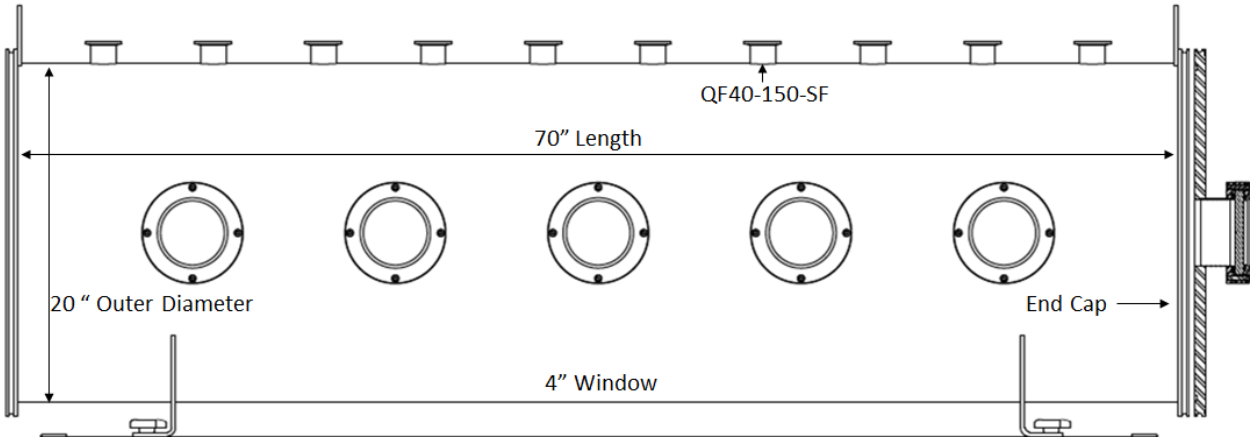

Figure 2.3: Schematics of one segment of CLaPTAM

2.2.2 Condensing Unit

Each of the individual chambers has its own condensing unit to regulate the temperature. These customized condensing units (Scientemp Corporation) use R404A as the refrigerant and is able to cool each 12 ft^3 (0.32 m^3) chamber to -20 ^oC. The compressed refrigerant from the pump

is directed into the chamber through one of the QF 40-150-SF ports to the evaporator where the heat exchange from the chamber to the refrigerant takes place. The warm refrigerant then is directed out of the chamber using the same port to the heat sink that is cooled by fanned air. This circulation continues until the temperature inside the chamber has reached the desired value. Three fans are positioned inside the chamber to help homogenizing temperature in the chamber. Figure 2.4 shows the change in the temperature of the CLaPTAM as the condensing units are on. It takes about 3 hours to cool down from room temperature of 21 ^{o}C to 0 ^{o}C about 10 hours for the chamber to be cooled down to -10 ^{o}C.

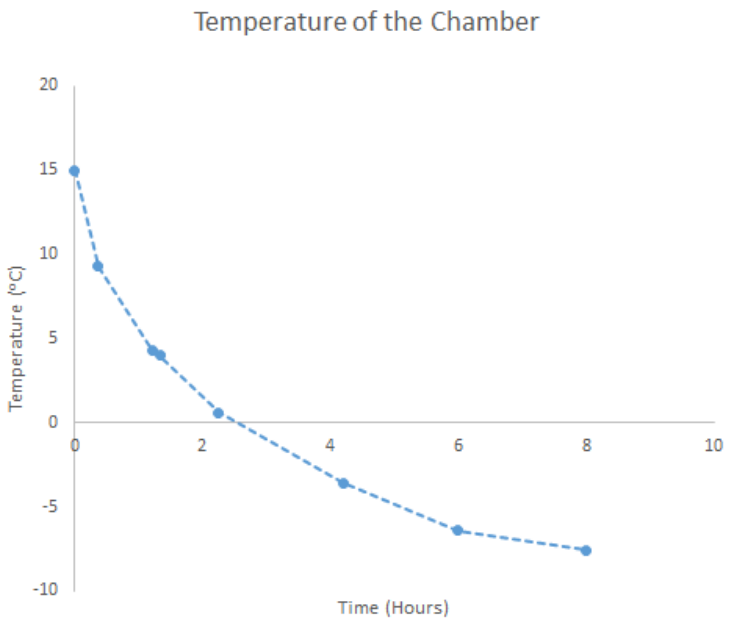

Figure 2.4: Change in temperature of CLaPTAM with respect to time.

2.2.3 Aerosol Generator

A cloud is composed of multiple aerosols with its size varying from 1μm to 120 μm [115, 116]. To mimic condensed aerosol media in the atmosphere such as fogs and clouds, CLaPTAM is equipped with a multiple aerosol generator. The multiple aerosol generator (Koolfog) produces 20 μm diameter droplets at a rate of 0.5 gallon per minute. In order to fill the chamber uniformly along the propagation axis, the main outlet of the multiple aerosol generator was divided into 6 evenly spaced outlets along the chamber. The fans mentioned previously distribute the aerosols uniformly along the entire length of the chamber.

2.2.4 Filament Beam Profiler

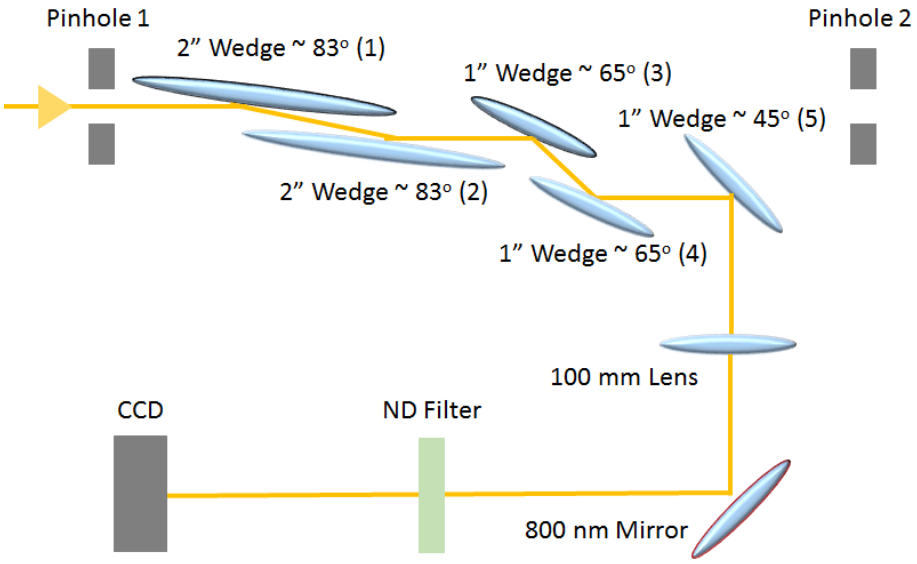

Figure 2.5: Schematics of multiple wedge grazing incidence filament beam profiler.

The grazing incidence filament beam profiler shown in Figure 2.5 was developed in the Laser & Plasma Laboratory by Khan Lim [114]. In order to save the optics from damaging due to the high intensity of the filament, the first 2" wedges have an angle of incidence (AOI) set to ~83^{o} to distribute the filament profile over a large area (8.2 time greater than initial area of the beam). The reflected beam (36 % for P-polarized light) from the first wedge was then sent to a second 2" wedge also set to ~83^{o}. The reflected beam from the second wedge then goes through the next two 1" wedges at 65^{o} of incidence angle that are ~ 1 % reflective. The beam was then sent to a fifth wedge at 45 ^{o} (~ 1 % reflectivity) through a 100 mm focusing lens to provide a 1:1 image of the filament profile onto a CCD camera (The Imaging Source DMK72BUC02). Neutral density filters were used to prevent the saturation of the CCD camera.

The grazing incidence filament beam profiler was fixed on a moving rail to measure the filament profile along its propagation inside the chamber (Figure 2.6).

Figure 2.6: Grazing incidence filament beam profiler on the rail inside CLaPTAM

2.2.5 Particle Size Analyzer

A Particle size analyzer (Malvern Spraytec) was installed to understand the propagating medium as well as to analyze the effect of the laser filament on the propagating aerosol medium after the interaction. The particle size analyzer uses laser diffraction to measure the size distribution of multiple aerosols from the scattered light. The particle size analyzer unit contains a transmitter module and receiver module. The transmitter module is a He-Ne laser with its maximum output power of 4 mW while the receiver module is a 36 element log-spaced array. The He-Ne laser beam is scattered as it passes through the analyzed particles as illustrated in Figure 2.7. The scattering angle of the beam is relatively larger for smaller particles than for the

larger particles. The receiver module analyzes the scattering pattern to provide the size distribution of the particles.

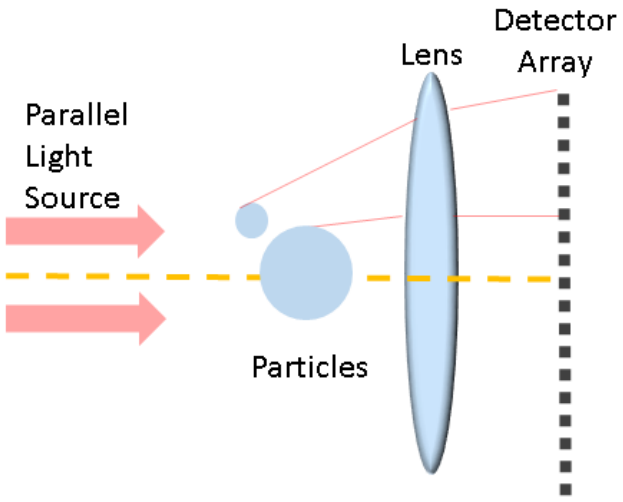

Figure 2.7: Basic principal of laser diffraction particle size analyzers.

Unlike the other particle size analyzers, the sample location of the particle size analyzer is in open air where the filament interaction with aerosols could take place. This allows a measurement of the propagation medium before and after the interaction with a laser filament.

2.3 Single Droplet Generator

In order to understand the filament propagation through concentrated aerosols such as clouds and fogs, it is important to first understand the fundamentals of filament-droplet interaction. Therefore, a piezo-electric drop-on-demand droplet dispenser (MicroFab) was used to study a single droplet interaction with a single filament. This droplet dispenser system

contains a pressure regulator, an electrical signal generator and a piezo-electric dispenser tip Figure 2.8.

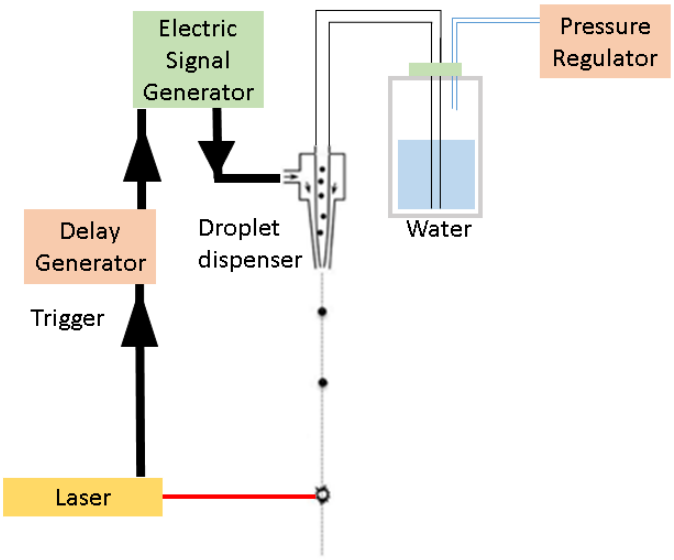

Figure 2.8: Schematics of droplet dispenser.

The droplet generator can be synchronized with the laser. The size of the droplet can be varied by changing pressure, input electrical pulse, and orifice diameter. Figure 2.9 shows an example of changing the droplet size by varying the input pressure to the droplet dispenser.

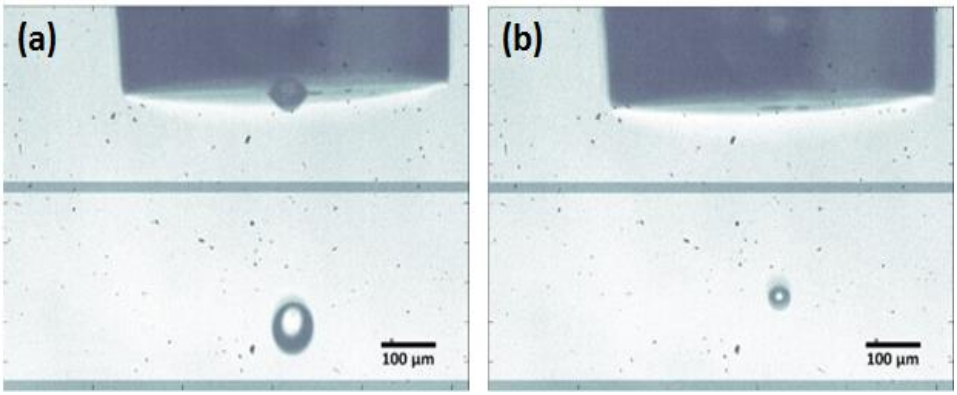

Figure 2.9: Droplet generation of (a) 75 µm (b) 40 µm droplet

The reproducibility of the droplet generator was measured using a microscope objective lens over 30 measurements. Changes in the size of the droplet (Δa), radial positioning (Δy), and propagation axis positioning (Δz) respect to the size of the droplet (50 µm) was measured to be $\Delta a/a < 0.03$, $\Delta y/a < 0.05$, $\Delta z/a < 0.03$ (Figure 2.10). Therefore, the size and the positioning of the aerosols were highly reproducible compare to the dimensions of the filament (~ 100 µm core, ~ 80 nm in length)

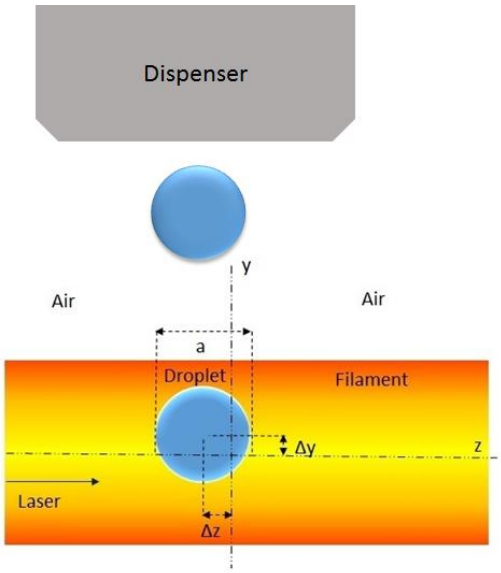

Figure 2.10: Schematic of a droplet interacting with filament.

3 INTERACTION OF A FILAMENT WITH AEROSOLS

The interaction of laser filaments with aerosols has been a subject of interest since the discovery of filamentation [7, 66, 117-120]. Current studies include the impact of filaments on aerosols such as water condensation [99, 100], air-flow motion [101], aerosol formation [102], aerosol explosion [103, 104, 121], and climate engineering [105]. In this chapter, the fundamentals of the interaction between a single filament and a single aerosol will be discussed.

3.1 Previous Studies

The transmission of laser beams through fogs and clouds is one of the main concerns for laser propagation through the atmosphere. In order to understand the effect of concentrated aerosols on the filament propagation as well as the effect of the filament on the propagation medium, the fundamentals of filament-aerosol interaction need to be understood.

The survival of a filament as it interacts with 50 and 95 μm diameter droplets was studied by Courvoisier *et al.* [49]. They positioned the droplets at the core of a filament and at the longitudinal location of 1m from the filament start location. Their results show that the filament was unaffected by the droplet and there was only a minor loss of energy in the beam (40 μJ). In addition, to effectively obstruct the core of the filament, black ink was added to the droplet. However, there was no significant difference between the transparent (pure water) and the absorbing (water with black ink) droplets. These findings show that blocking the core of the filament using an obstacle has negligible impact on the filament propagation, which strongly supports the replenishment of the filament by the surrounding energy reservoir. To evaluate the

filament survival limits, the effect of aerosol concentration was examined by the same group. They sent filament through an open chamber (35 cm long) with the droplet concentration ranging from 0 to 6x 10^{15} cm^{-3} with a droplet mean diameter of 4 μm and measured the transmitted energy. No significant changes in the length of the filament was visible up to the cloud optical thickness τ [τ = ln(1/T), where T is the transmission of HeNe] of 1.2 (10^5 droplets/cm^3) and the filament stopped propagating for an optical thickness of 3.2 (4 x 10^5 droplets/cm^3), due to the elastic scattering losses caused by the droplets on the energy reservoir.

The impact of ultrafast lasers and filaments on the droplet has been studied by several research groups [103, 104, 121, 122]. During the interaction of a laser with a droplet, light can be focused within the droplet, inducing an internal plasma if the irradiance is large enough. This plasma can lead to the deformation and even the fragmentation of the droplet as demonstrated by Efimenko *et al*. [104]. However, our group has shown the plasma generation at the front surface of the droplet as the laser filament interacts with the droplet [122]. The difference between these two results will be discussed in Section 3.4.

In many of the studies, the initial characterization of the filament was not provided. Moreover, no studies have examined the implication of the droplet position with respect to the filament in both radial and propagation axis on the filament characteristics. Early time (within 50 ns after the interaction) measurements of the droplet explosion can provide information on the amount of energy dissipated by the filament in the droplet by analyzing the shockwave produced by this interaction. The influence of the droplet on the filament at different spatial locations relative

to the filament will provide information on the survival of the filament with respect to its spatial energy distribution.

3.2 Energy Deposition within the Droplet

Previous studies have suggested that as the filament interacts with a single droplet, it suffers a minor energy loss and has negligible impact on its propagation (Section 3.1). During this interaction, the droplet explodes and ultimately results in the formation of sub-micrometric droplets or nano-aerosols. A sudden energy deposition in a medium induces a strong explosion resulting in a flow of a pressure wave, also known as a shockwave, that propagate through the medium starting from the location where the energy is released [123]. To quantitatively measure and understand the underlying physical mechanisms behind the energy loss, the shockwave expansion from the front-surface plasma created on the droplet was analyzed in the first ~ 50 ns.

3.2.1 Sedov-Taylor Analysis of Shockwave

When an ultrashort laser pulse with high intensity is focused on the surface of a target, a plasma is generated. The expansion of the laser-produced plasma in air (1atm) generates a strong shock at the interface, generating a shockwave. This impact of the plasma on the ambient air acts as a supersonic piston and this results in a discontinuity of the pressure (the density of air). Due to the relationship between the refractive index and the density of air, a discontinuity in refractive index is evident and it can be used to image shockwave fronts [124, 125].

Shockwaves have been observed during the filament interaction with solids, liquids, and gases [126-128]. Assuming that the release of the energy is an instantaneous point source, the

spatial distribution of the flow variables are in a same form in time (self-similar flow). The radial expansion of the shockwaves with respect to time can be fitted by the Sedov-Taylor equation and be used to solve the solutions to the self-similar problem and thus extract the laser energy deposited on the target sample [64, 129, 130]. The Sedov-Taylor blast wave equation for spherical shockwave expansion in free space is expressed as [131, 132]:

$$R = A\left(\frac{E}{\rho}\right)^{\frac{1}{5}} t^{\frac{2}{5}} \qquad (3\text{-}1)$$

where R is the radial expansion (m), A is a constant close to 1 [123], E is the initial energy (J) released as the cause for the shockwave, ρ is the density (kg/m^3) of the propagation medium and t is the time (s). A time varying radial shockwave expansion with its initial energy of 1, 2, and 5 joules is demonstrated in Figure 3.1. The speed of the radial expansion (Figure 3.1) of the shockwave decreases as the time increases (speed α $t^{-3/5}$). Measuring the radial expansion of the shockwave at different times can be used to derive the initial energy that is responsible for the shockwave generation.

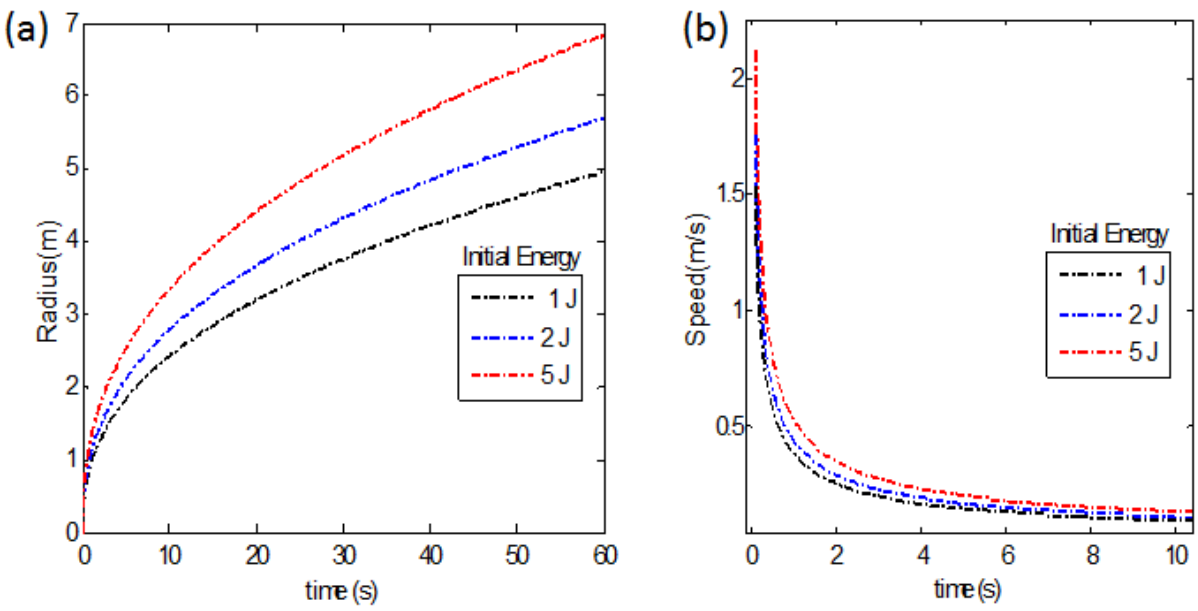

Figure 3.1: (a) Radial expansion and (b) speed of a shockwave in air with initial energy of 1 (black), 2 (blue), 5 (red) J.

3.2.2 Shadowgraph Technique

Picosecond multichannel interferometry and shadowgraph technique have been used to image temporal evolution of plasmas as well as shockwaves generated form laser induced plasmas [56, 64, 133, 134]. In this thesis, shadowgraph technique is used to image shockwaves generated from the filament-aerosol interaction.

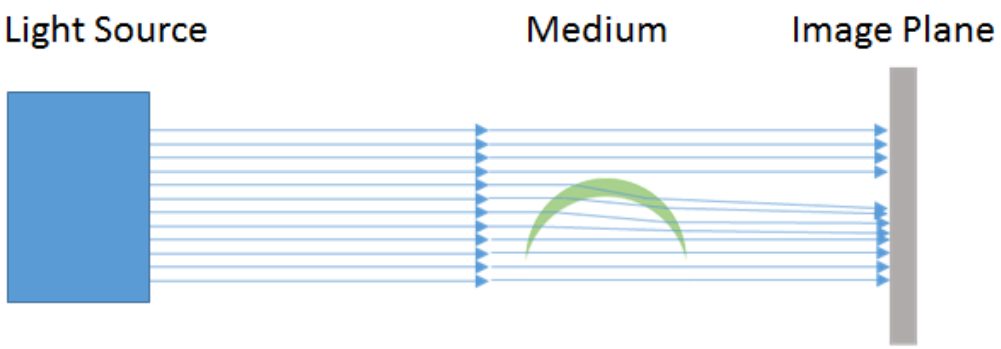

Figure 3.2: A schematic of shadowgraph imaging system.

The shadowgraph technique is an optical method to capture the variations in a transparent medium. Just like an ordinary imaging system, shadowgraph imaging system consists of a light source, a medium and an imaging source. However, to capture a fast moving flow, like a shockwaves, an ultrafast laser pulse can be used as a light source. The pulse width of the light source (laser pulse) determines the temporal resolution of the images if it is shorter than the gate width of the imaging source. Therefore, by using a 50 fs laser pulses from MTFL (Section 2.1), 50 fs temporal resolution is achieved.

As the laser pulse propagates through the medium with a different refractive index, the laser beam is deflected from its original path to the image plane (Figure 3.2). The deflection of the initial beam will result in the absence of the light rays entering the pixel arrays of the detector. This localized change in the intensity of the laser pulse visualizes the outline of the change in refractive index of the medium as bright and dark lines.

Figure 3.3 shows an example of a shadowgraph image from the interaction of a laser induced filament (2.2 mJ, 50 fs, 800 nm, 1.2 m external focusing) with a water droplet, taken at 10 ns delay. The droplet, plasma and the outlines of the created shockwave are clearly visible.

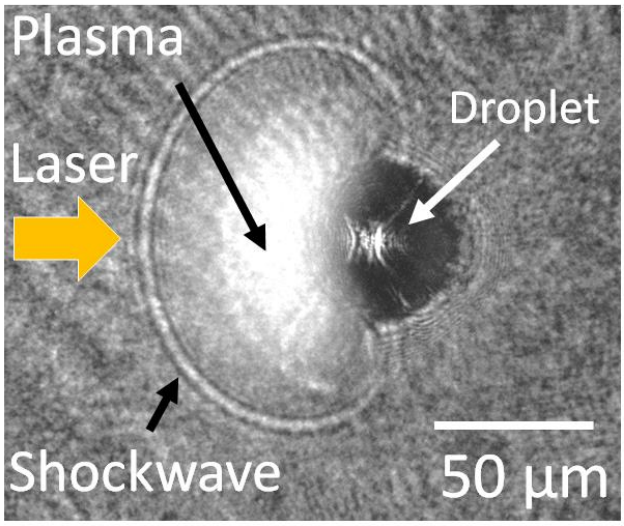

Figure 3.3: Example of a shadowgraph image of shockwaves created during the interaction of a water droplet with a filament (2.2 mJ, 50 fs, 800 nm, and 1.2 m external focusing), taken at 10 ns delay

3.2.3 Experimental Setup

The experimental setup of the shadowgraph imaging system is shown in Figure 3.4. 4 mJ, 50 fs, 800 nm pulses at 10 Hz were used from the output of the MTFL (section 2.1). The pulse was split by 90%/10% with a non-polarizing beam splitter to generate the filament and the probe beam for the shadowgraph imaging system, respectively. The probe beam (0.4 mJ) was first sent to a fine precision delay stage (14 ns range with 100 ps mechanical resolution). The beam was

frequency doubled by a BBO crystal in order to transmit the probe beam but block the scattered 800nm light at the CCD equipped with a 400 nm interference filter. The frequency-doubled beam was then sent to the coarse resolution delay stage with 42 ns range and 14 ns increments. The shadowgraph image of the droplet was imaged onto the CCD by illuminating it with the delayed probe beam. A 1.2 m focusing lens was used to induce filamentation of the pump beam (2.2 mJ after the light valve), to interact with the single droplet generated by a piezoelectric droplet generator (see Section 2.3).

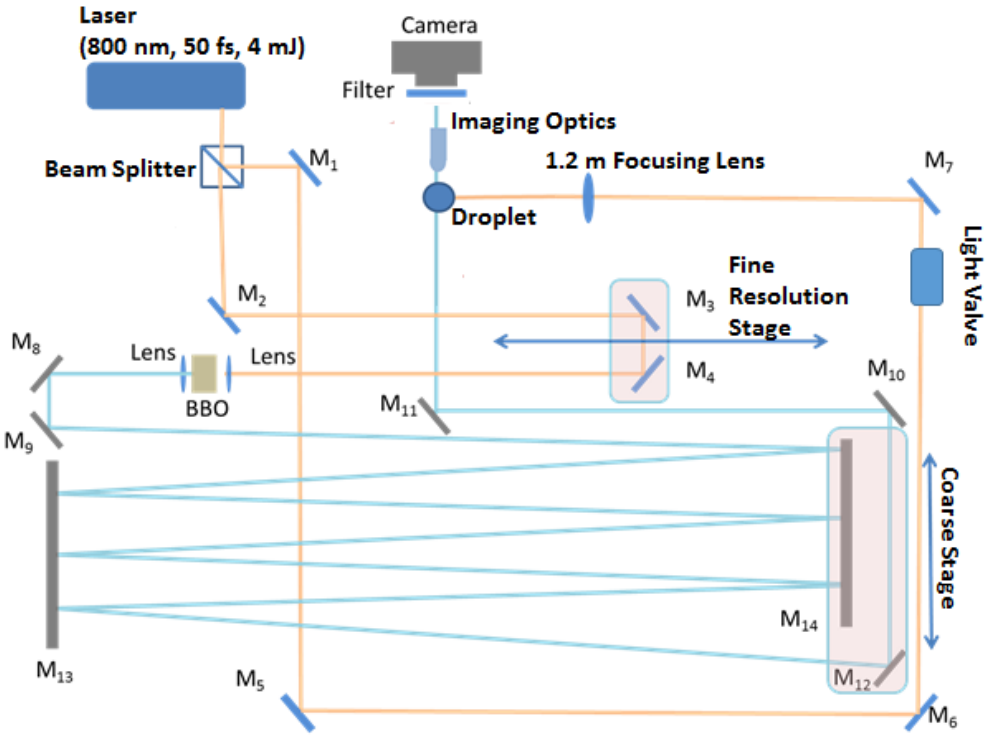

Figure 3.4: Experimental setup of shadowgraph imaging system for droplet explosion

The droplet generator was positioned on a xyz translation stage where the dispenser tip of the droplet generator can be precisely positioned on top of the filament (Figure 3.5). A 48 μm diameter droplet was generated and placed at the core of the filament in the middle of its propagation.

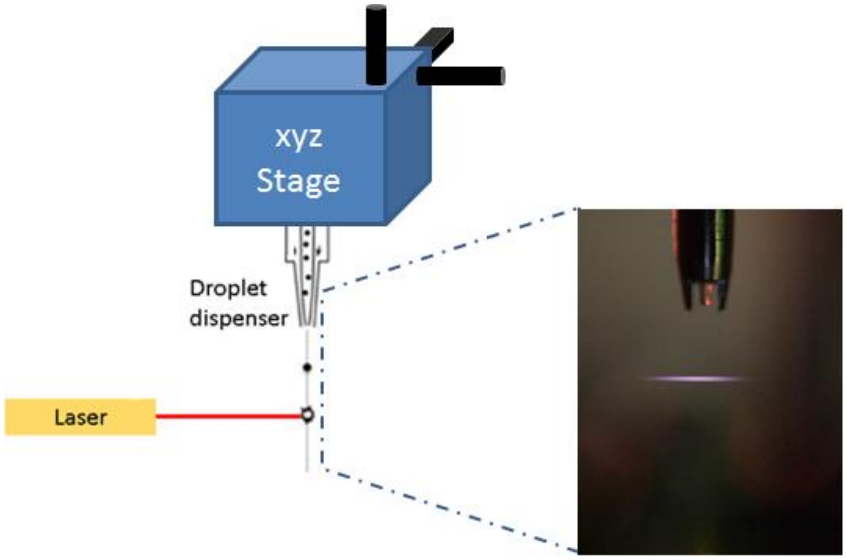

Figure 3.5: Experimental setup of the droplet generator positioned on top of the filament using xyz linear translation stage.

3.2.4 Measurement of the Energy Dissipated During the Interaction

The amount of dissipated laser energy during the filament-aerosol interaction produces the plasma that generates a shockwave in air traveling normal to the surface of the droplet in the opposite direction with respect to the laser pulse. The shockwave generated during the filament-aerosol interaction is used to measure the dissipated laser energy to the droplet.

The radial expansion of the shockwave was measured from shadowgraph images taken at different delays and fitted against the Sedov-Taylor equation (Equation 3-1) to derive the dissipated energy of the filament in the droplet (Figure 3.6).

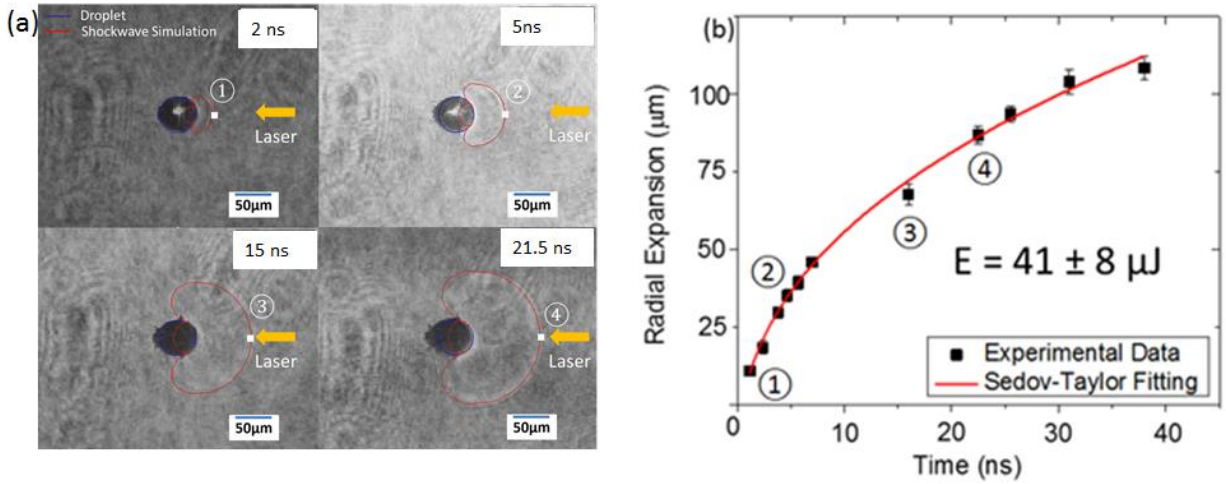

Figure 3.6: (a) Simulation of Sedov-Taylor equation shown on images taken at delays 2, 5, 15 and 21.5 ns (b) Radial expansion of the shockwave generated in filament-droplet interaction with respect to time.

For statistical analysis, thirty images of the shockwaves were taken at each delay. The calculated energy loss during the interaction was found to be 41 ± 8 µJ.

The initial filament beam profile was measured prior to its interaction with droplets to understand how much of the energy is encompassed within the area of the interaction. The grazing incidence filament beam profiler (Section 2.2.4, Figure 2.5) was used along the propagation axis of the filament. The laser pulses (2.2 mJ, 50 fs) were focused by a 1.2 m focal length lens to generate a single filament. The peak fluence as well as the spatial extent (FWHM)

of the core of the filament were measured throughout the propagation and are shown in Figure 3.7. A sudden decrease in the spatial extent of the laser beam occurs at position ~ 80 mm before the focal plane (at 1.2m). This sudden decrease is due to the Kerr self-focusing of the beam and can be described as the collapse location of the filament. As the size of the beam decreases, the intensity of the beam increases. The CCD camera was calibrated in energy by measuring the response of the pixel counts with respect to a known input energy. Since the temporal profile of the filament changes during its propagation (Section 1.2.5) the pulse width is unknown. Therefore the calibrated peak energy value of the filament is given as peak fluence (J/cm^2). The region of interest where the filament-droplet interaction takes place throughout this chapter ranges from -100 mm to 20 mm from the geometrical focus.

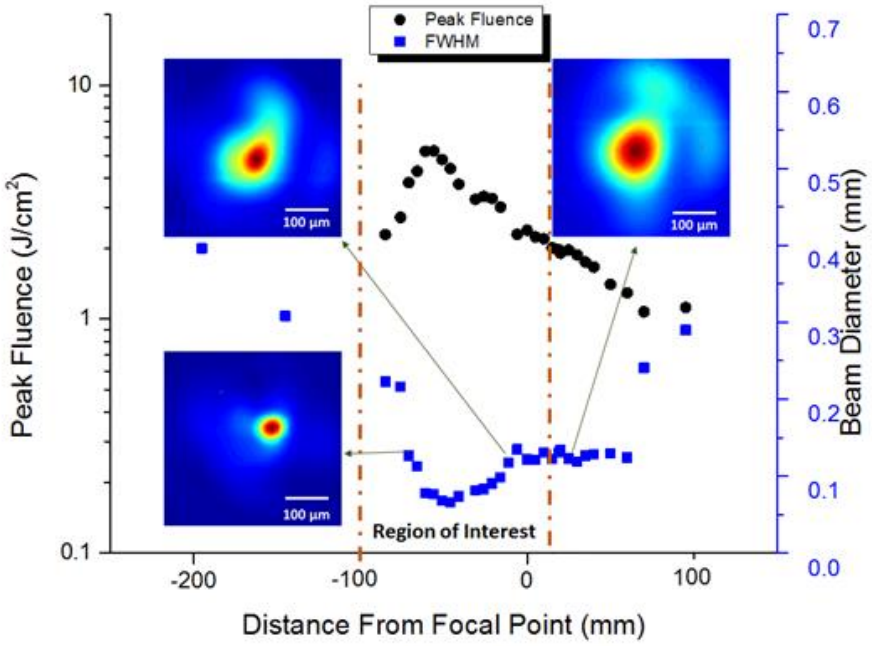

Figure 3.7: Measurement of the filament profile along the propagation axis.

The initial fluence of the beam propagating in free air was measured to be 54 ± 4 μJ for 48 μm diameter disk at the propagating location of droplet-aerosol interaction (Figure 3.8). Since the absorption coefficient of water is 0.02 cm^{-1} at 800 nm, the energy lost due to linear absorption of 48 μm water is 0.01% [135]. Therefore it can be concluded that most of the energy within the filament core that is intercepted by the droplet has been consumed by plasma generation (76 % ± 15%). The rest of the energy is either scattered or transmitted.

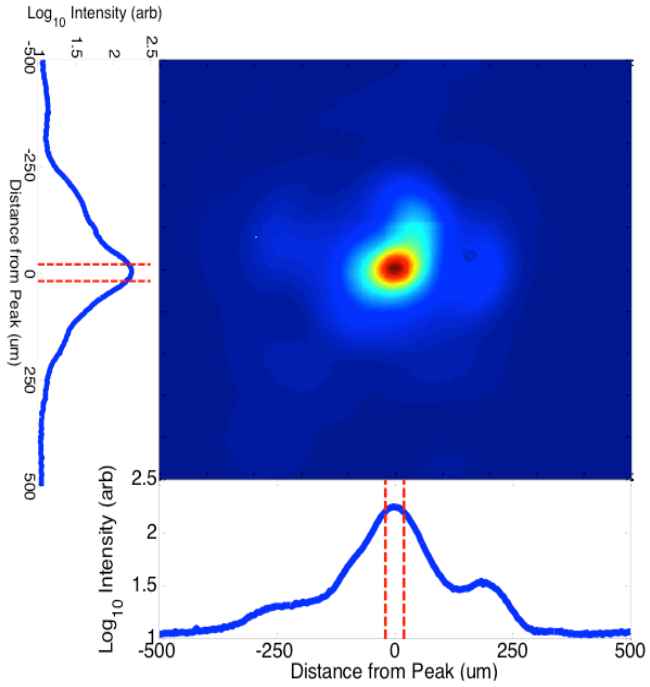

Figure 3.8: Filament beam profile at the propagation axis where droplet interaction takes place (red dotted lines indicate the size of the droplet)

To see the impact of the initial laser energy on the amount of energy dissipated in the droplet, the initial laser input energy of .5, 1.0, 1.6, and 2 mJ was used to interact with the

droplet. The radial expansion of the shockwave was measured at a given delay (t = 31 ns). For the initial input energy of 0.5, 1.0, 1.6, and 2 mJ, the radial expansions of the shockwave were 105 ± 2, 106 ± 2, 106 ± 2, and 105 ± 2 μm respectively. This indicates that the peak intensity of the filament core that is interacting with the droplet doesn't change with the initial laser energy, verifying the phenomenon of intensity clamping (see Section 1.2.2).

3.3 Effect of the Droplet on the Filament

Multi-photon is one of the major causes of energy loss for a filament propagating in clean air. When diffraction overcomes Kerr self-focusing to the point that there is not enough energy left in the photon bath to maintain the balance, the filament is terminated as the beam diverges. This is called in this work the "filament end location". However, in the presence of aerosols, most of the energy that is interacting with the droplet is dissipated in the plasma generation on and in the droplet. The following section will discuss the changes in the characteristics of the filament, such as start and end points, due to the interaction with an aerosol.

The nitrogen emission was used as the proxy for the existence of a filament (see Section 1.2.4). The SLR camera was replaced with an ICCD to minimize the intake of the background noise by having a short gate width that only opens during the filament formation. The ICCD was used to image the nitrogen emission (200 accumulations at 5 μs gate width) from the side in the experimental setup discussed in Section 3.2.3 (see Figure 3.5). For this experiment the droplet location was varied along the propagation axis from – 90 to 0 mm relative to the linear focal plane with a step size of 10 mm. The images of the nitrogen emission from the filament, as the

droplet is positioned along the propagation axis, are shown in Figure 3.9 where the symbol ‘X’ indicates the location of the droplet.

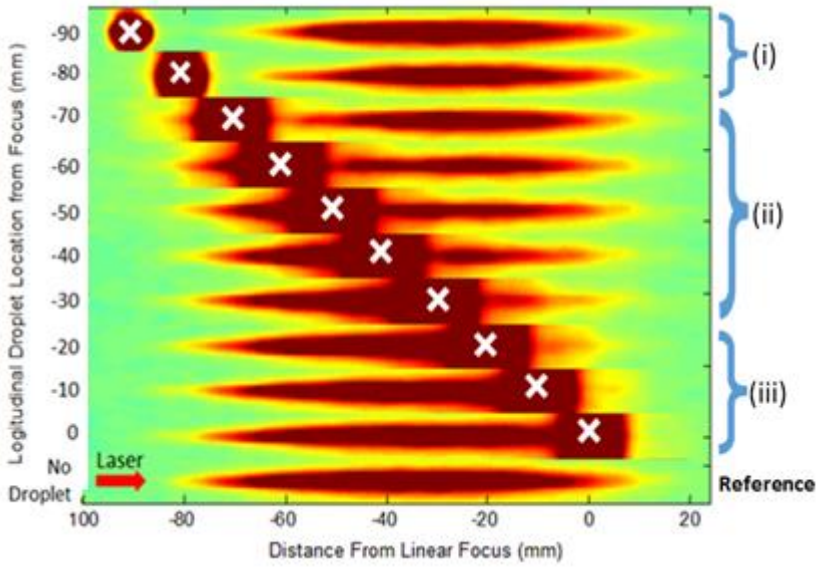

Figure 3.9: Nitrogen emission images from the filament as the droplet is moved along the propagation axis. The symbol X represents the droplet location.

As the droplet interacts with the filament along the propagation axis, three different regimes of modifications of the filament were observed (Figure 3.9): (i) a shift in collapse location when the droplet was positioned prior to the initial self- focusing location without the droplet (-80 mm), (ii) filament reformation for the droplet location from -70 to -30 mm, and (iii) filament disruption when the droplet was positioned near the geometrical focal plane (-20 to 0 mm).

The energy loss during the interaction of the filament with droplet (41 ± 8 μJ, Section 3.2.4) is the primary reason for the observed changes. From previous studies, the role of the

energy reservoir on the reformation of the filament after interacting with an obstacle is well understood [49, 64, 66]. However, the influence of the location of this interaction on the characteristics of the filament has not yet been studied. To understand the effect of the energy loss on the shift in the collapse and end locations, numerical simulations based on one-dimensional NLSE were performed [136].

3.3.1 Simulation Results

The initial parameters of the pulse for the simulation were set to 0.73 mJ energy, 50 fs duration, 800 nm central wavelength, 5 mm in diameter on a Gaussian profile focused by a 1.2 m positive lens. For the simulation energy, a reduction factor of 3 was used [136]. Since most of the filament energy that is interacting with a droplet is lost, a Gaussian gradual mask with 50 μm width at 1/e was used in place of a droplet to simplify the simulation (Figure 3.10). Gaussian gradual mask was chosen over a binary mask to minimize any instability in the simulation by minimizing numerical discontinuities.

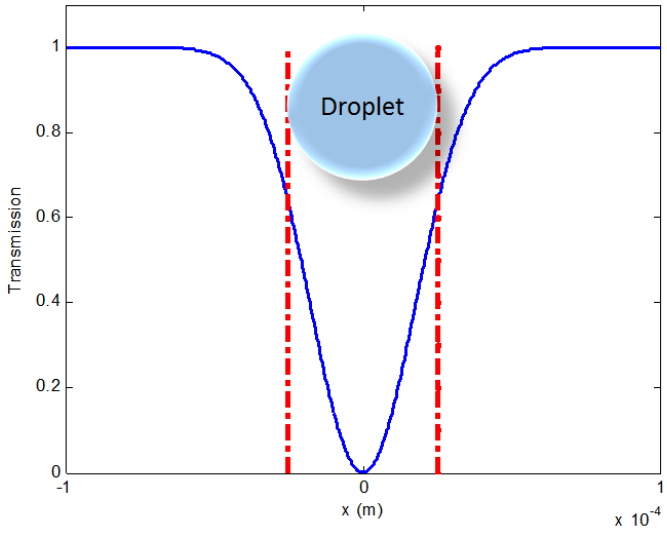

Figure 3.10: Gaussian gradual mask with 50 μm width at 1/e

The simulation results showed that a free propagating filament of ~ 270 μm (FWHM) was formed at a location of 80 mm prior to the linear focal plane. The Gaussian gradual mask was positioned along the propagation axis from -130 mm to -20 mm from the linear focal plane with 10 mm increments. Figure 3.11 (a) and (b) compare the filament beam profile with and without the droplet at -130 mm, confirming the filament energy loss with in the interaction region. The ring shaped filament profile at this point in space still has enough power to induce Kerr self-focusing recovering its initial shape further down propagation (Figure 3.11c and d).

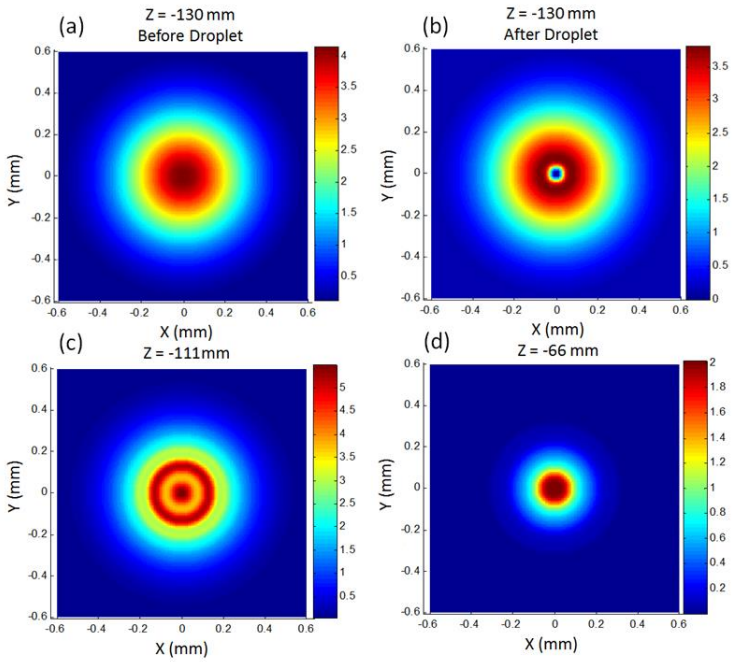

Figure 3.11 Beam profile of the laser at (a) -130 mm without the Gaussian gradual mask, (b) -130 mm with the mask, reforming at (c)-111mm and (d) -66 mm from the linear focal plane.

Simulation and experimental results were compared to understand the effect of the energy loss from the droplet-filament interaction on the shift in collapse and end location of the filament. The shift (normalized to the maximum shift to compare the trend) in the collapse location of the filament with respect to the droplet location along the propagation axis is shown in Figure 3.12 (b). The change in collapse location is definitely visible for both simulation and experimental results where the droplet is located prior to the reference collapse location (without the droplet). A gradual decrease in the shift of the collapse was visible as the droplet was positioned even farther away (-130 ~ -90 mm) from the linear focus. Figure 3.12 (b) shows the experimental and simulated shifts in the collapse location are in agreement with each other. It

also confirms that as the filament energy loss in interaction with the droplet increases, the shift in collapse and end locations also increases.

The shift in the end location was normalized to the maximum shift as well to compare the trend between the experimental and simulation data and was plotted for both experimental and numerical values. Unlike the shift in the collapse location, the shift in the end location was visible for any droplet location as it is shown in Figure 3.12 (c). The energy loss was calculated by dividing the energy after the droplet by the initial energy. Therefore the energy loss is the sum of the energy loss from the filament-droplet interaction and from the different intrinsic loss channels in filamentation. The simulation clearly reproduces the behavior obtained from the experiment and the normalized energy loss also follows the experimental and simulation shifts.

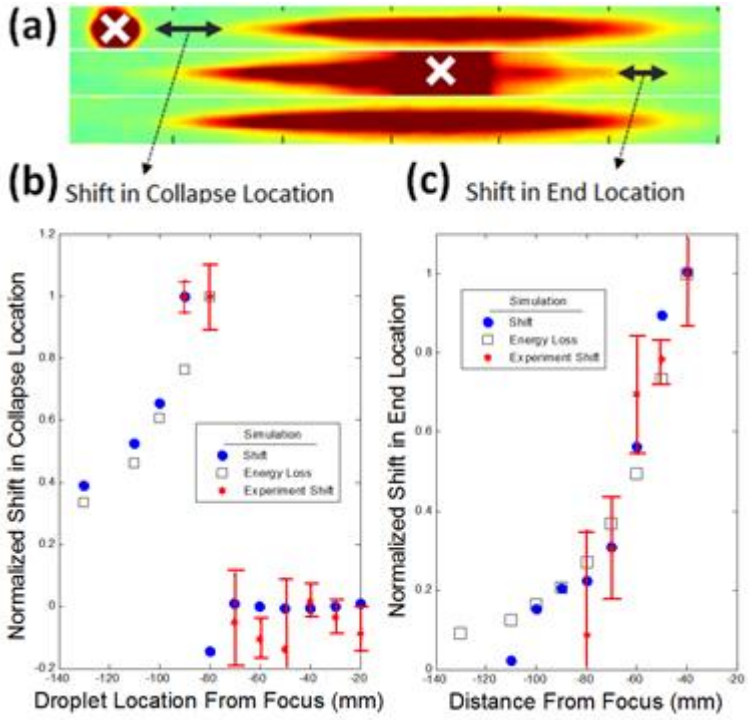

Figure 3.12: (a) Nitrogen emission from the filament with arrows indicating the shifts in collapse and end location. Simulation (circle) and experimental (star) values of the shift in (b) collapse location and (c) end location of the filament. Simulated values of the energy loss (square) at the interaction are shown for both (b) and (c)

3.3.2 Filament Obstruction by an Off-Axis Droplet

To understand the influence of the droplet position along the radial profile of the filament, the 50 μm diameter droplet was fixed on a plane 20 mm after the filament collapse point and then was precisely positioned at 0 to 60 μm, with respect to the propagation axis, on the radial axis.

As the droplet is located at the center of the filament core, the energy loss during the interaction is the greatest since the center of the filament core carries the peak intensity. This stops the filament temporally as shown in Figure 3.13.However, since the energy reservoir has enough power to induce Kerr self-focusing to overcome the diffraction, the filament re-collapses around -40 mm from focal plane.

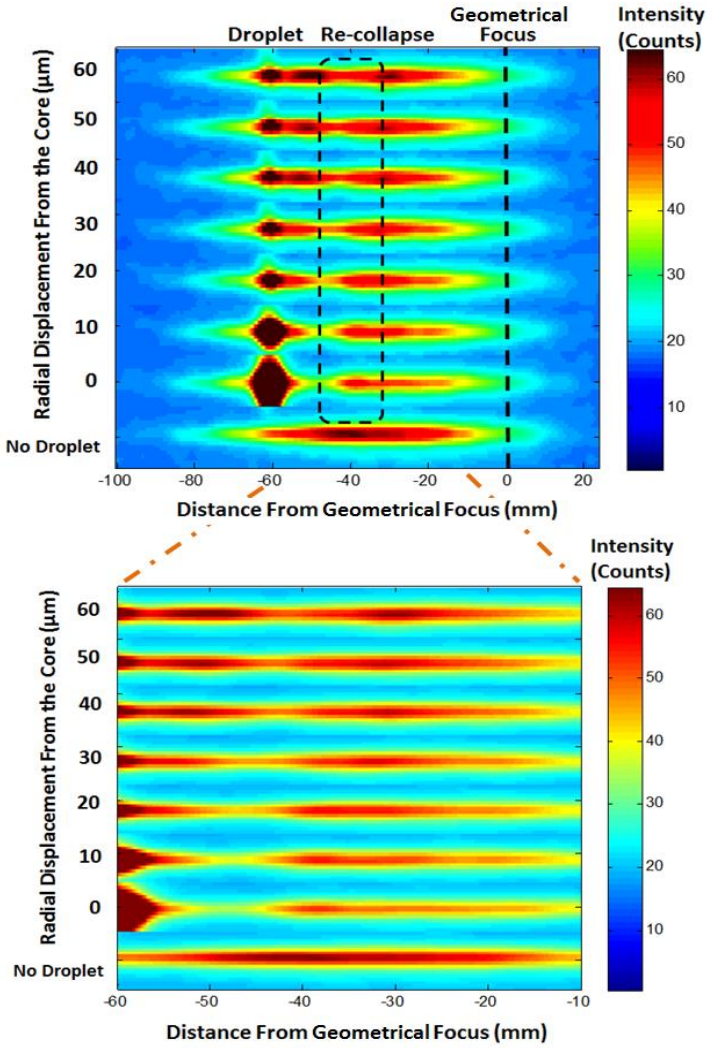

Figure 3.13: Nitrogen emission of filament as the droplet is positioned along the radial axis of the filament

As shown in Figure 3.13 the discontinuity in the filament shortens as the droplet is positioned away from the center of the filament core. When the droplet is located at the center of the filament, the filament discontinues right after the droplet. However, as the droplet is positioned away from the center, the filament survives until the discontinuity takes place. The filament then regains its initial profile down the path where re-collapse takes place.

The energy loss during the filament-droplet interaction can be measured using the Sedov-Taylor equation (see Section 3.2.1).The energy dissipation of the filament on to the droplet is proportional to R^5, where R is the radial expansion of the shockwave. To study the energy dissipation along the radial axis of the filament, the expansion of the shockwave generated on the droplet at a fixed delay of 10 ns is shown in Figure 3.14. As the droplet is positioned away from the core of the filament, the radial expansion of the shockwave decreased indicating a smaller amount of energy loss.

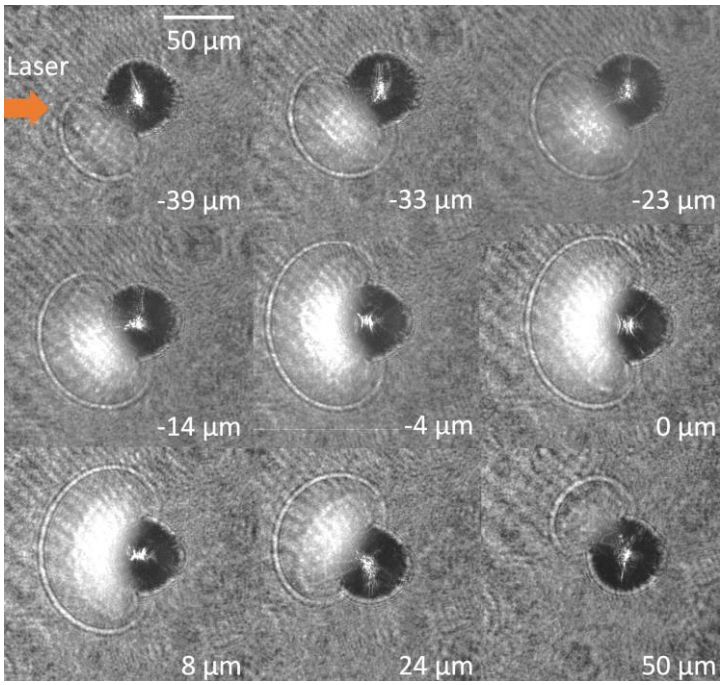

Figure 3.14: Shadowgraph images of shockwaves as the droplet is located along the radial axis of the filament. The values indicate the distance from the center of the filament core

3.4 Effects of an Ultrafast Laser Pulse on a Single Water Droplet

As the laser filament interacts with a single droplet, sequence of complex processes occur (Figure 3.15). At very early times, the leading edge of the pulse with intensity lower than the ionization threshold of water refracts at the surface of the droplet and gets focused inside (Figure 3.16). As the intensity of the pulse increases in time, it overcomes the ionization threshold of the water surface, creating a plasma at the front surface of the droplet (see Section 3.2.4). The amount of dissipated laser energy to produce the plasma generates a shockwave in air traveling normal to the surface of the droplet in the opposite direction with respect to the laser pulse.

However, the refracted leading edge of the laser propagates and focuses inside the droplet towards the back surface, generating plasma.

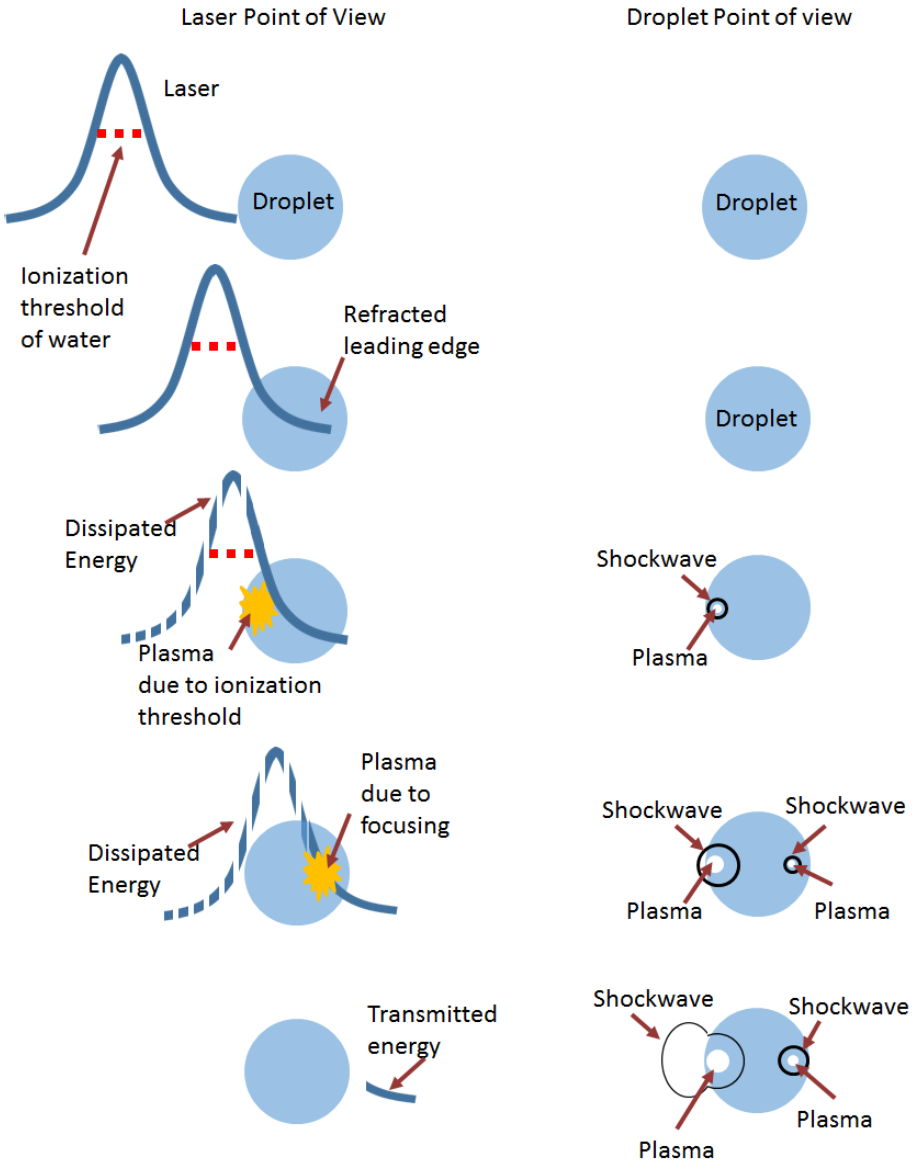

Figure 3.15: A complex sequence of laser filament interacts with a single droplet.

A Ray tracing was performed to understand the geometric beam path of the transmitted laser pulse (leading edge). The micro-sized water droplet can be compared to a spherical lens with a refractive index of 1.3. To simplify the calculation, a Gaussian profile (100 μm FWHM, 1 W/cm^2) was used. The diameter of the droplet was also set to be 100 μm with the refractive index of 1.3. The path of the laser as it interacts with the water droplet is shown in Figure 3.16. Transmission and reflection coefficients are taken into account for both front and back surface of the droplet. As the light propagates through the water droplet, a strong focusing at the back of the droplet was visible.

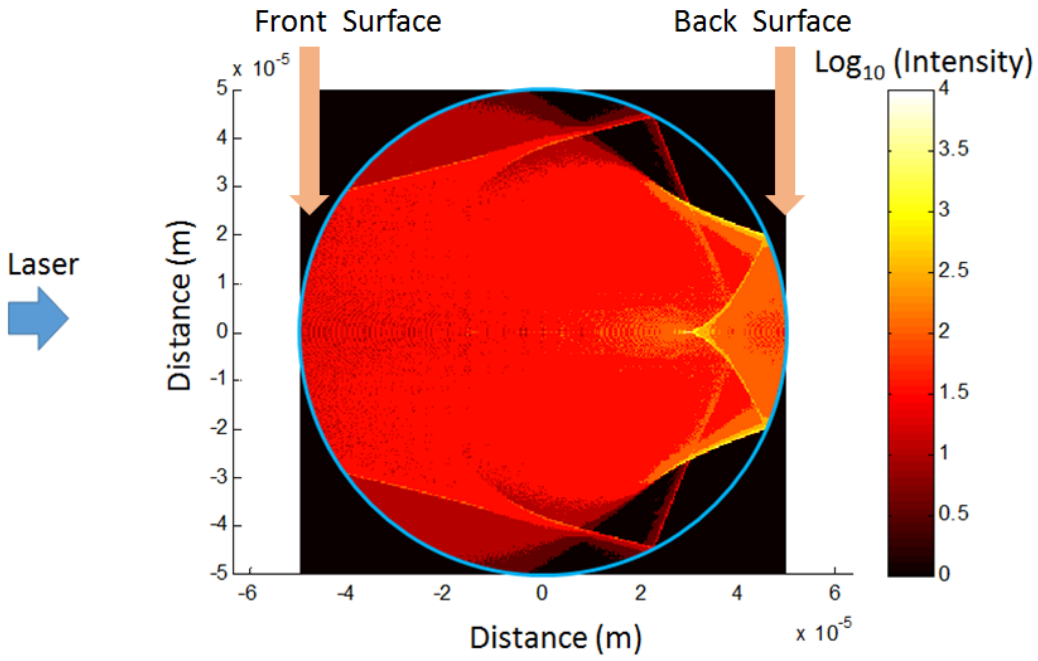

Figure 3.16: Geometric ray tracing of a CW beam propagating through a 100 μm diameter water droplet.

3.4.1 Internal Plasma Generation

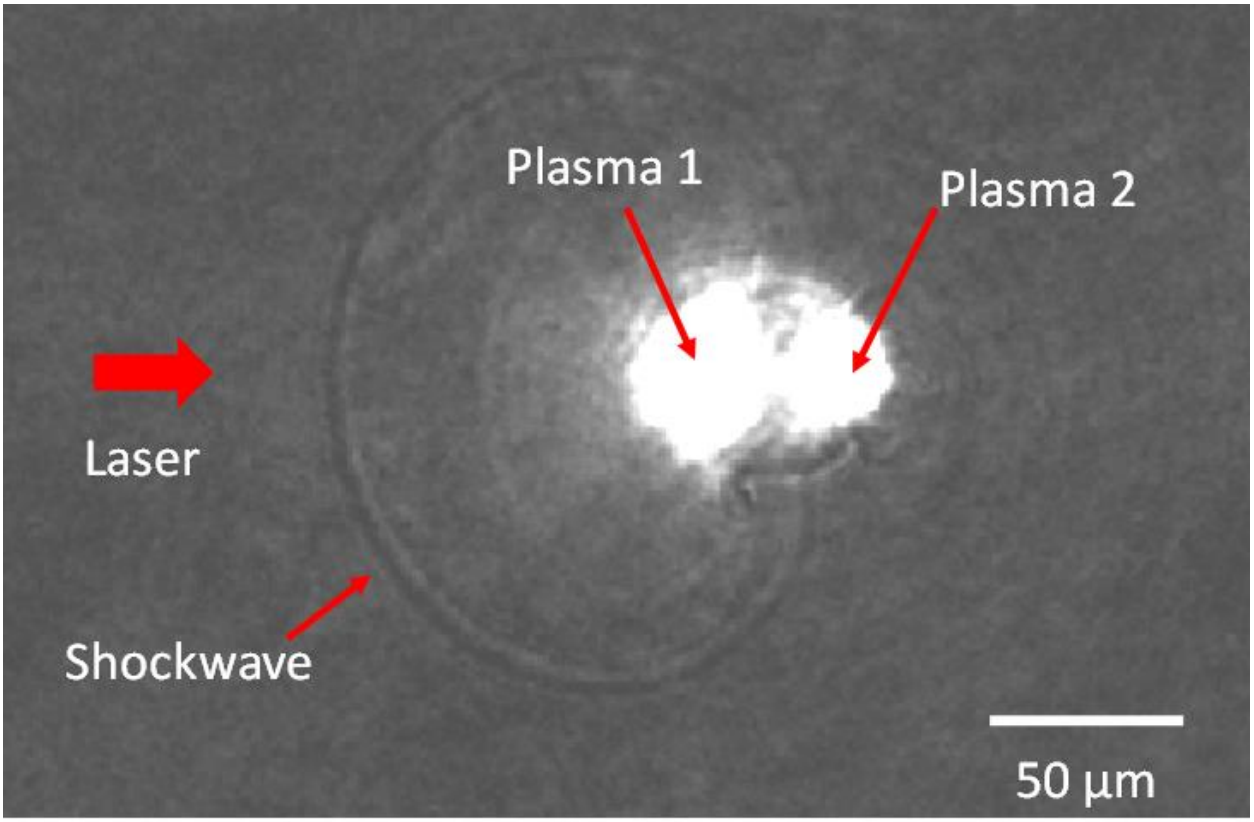

Figure 3.17: Shadowgraph image of a single droplet interaction with a single filament with low contrast

Figure 3.17 shows the plasma generation from two different sources. A portion of the leading edge of the pulse (below plasma threshold) is transmitted within the droplet where it is focused to a geometrical focus as described in Section 3.4. The remaining of the pulse is then blocked at the surface to form the surface plasma as described in previous sections. This results in plasma and shockwave generation at the front surface of the droplet (Figure 3.17). To support

the idea of two plasma sources, two pulses with different initial laser energies, have been interacted with single droplets: either with the peak laser intensity below or above the surface plasma threshold (~10 TW/cm^2 at 532 nm, 100 fs [104, 137], 18 TW/cm^2 at 795 nm, 120 fs [138]).

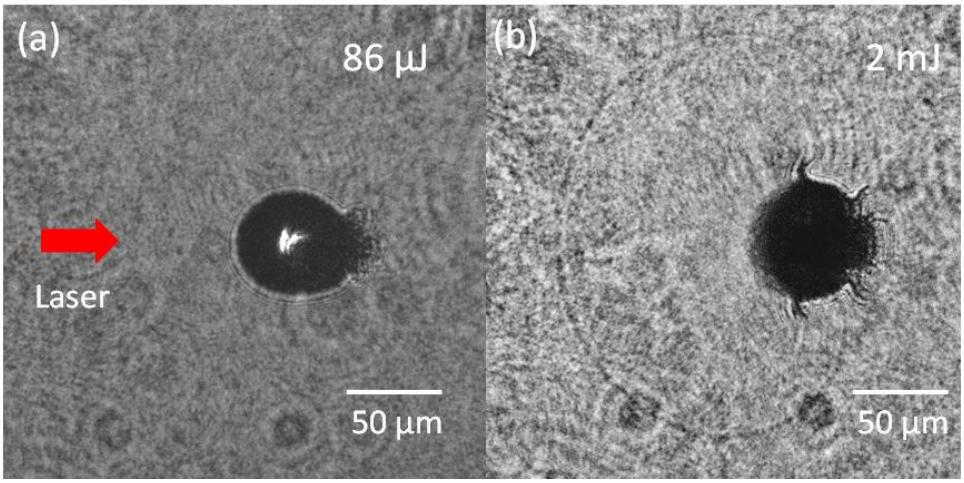

Figure 3.18: Shadow graph image of droplet interaction with ultrashort lasers with the initial energy of (a) 86 μJ and (b) 2 mJ with 1.2 m external focusing

For the initial laser beam with 86 μJ (1.72 GW), which is well below the critical power, the deformation is only visible at the back surface of the droplet (Figure 3.18 a). The peak intensity of the pulse does not have enough intensity to ionize the front surface of the water. However, it is focused in the droplet at the location described previously in Section 3.4, generating a plasma. However, when the pulse interacting with the droplet has enough intensity to ionize water at first contact, the surface plasma is induced on the first contact surface (Figure 3.18 b).

3.4.2 Droplet Explosions

Intense vaporization of the water particles from laser-droplet interaction leads to a droplet explosion. Depending on the initial parameters of the laser and the droplet size, the time scale for the formation of the fragments varies. As it can be seen in Figure 3.19, the 56 μm droplet fragments into nano-sized particles in a time scale of 5 μs.

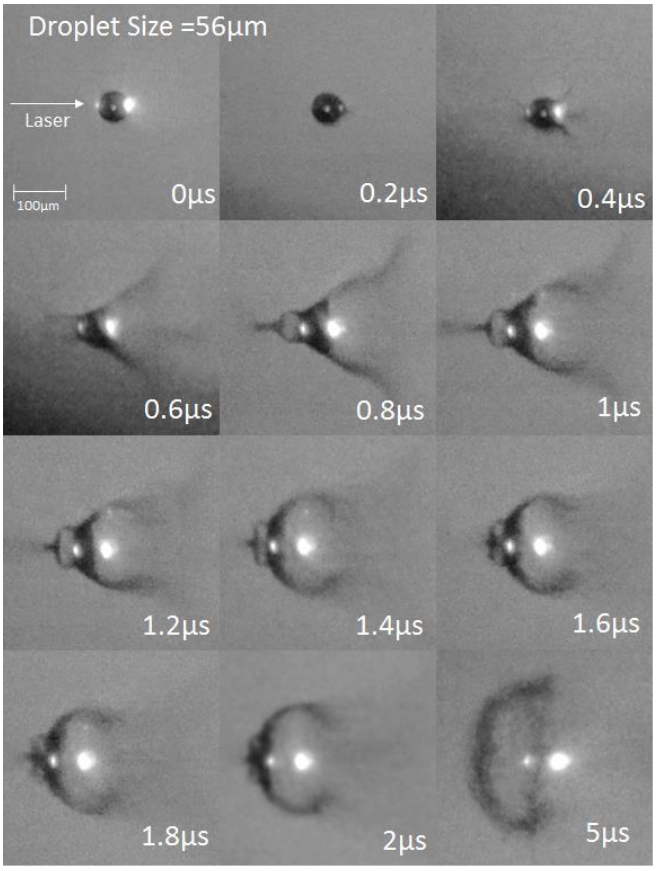

Figure 3.19: Shadowgraph images taken at different times of a 56 μm droplet located at 15 mm prior to the focusing plane, interacting with 100 fs laser pulses focused with a 250 mm focal length lens with input energy of 0.78 mJ.

3.4.3 Particle Size Distribution

As mentioned earlier in Section 1.3.3, a filament can be used to induce water condensation. Filament induced water condensation experiments showed a growth of the droplet sizes and a large increase in nano-sized aerosols [108, 110]. However, the fundamentals of the filament assisted water condensation is not fully understood yet.

An experiment was conducted to understand the increase in the nano-sized aerosols. A stream of single droplets (with a nominal diameter of 63 μm) was positioned within the measuring field of view of the particle size analyzer. The particle distribution was centered at 60 μm with a variance of 2 μm as shown in Figure 3.20.

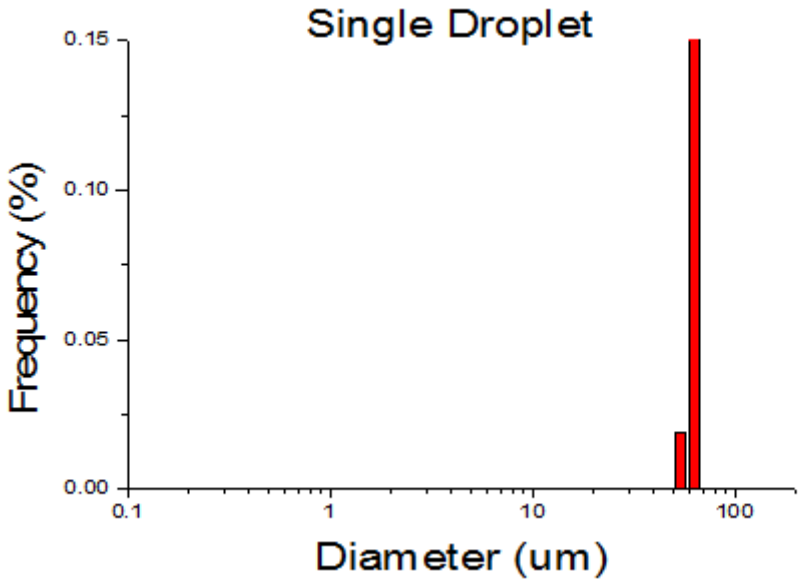

Figure 3.20: Particle size distribution of droplets before the filament-droplet interaction.

The measured particle size distribution shows that the droplet dispenser is generating a quasi-monodisperse train of droplets. When the filament interacts with the droplets, this distribution is modified.

An ultrafast laser pulse with 5 mJ, 50 fs pulses at 800 nm was focused with 1.2 m focusing optics to induce a single filament. The filament-droplet interaction fragments the droplet into smaller aerosols with a size distribution centered at 400 nm with a variance of 100 nm.

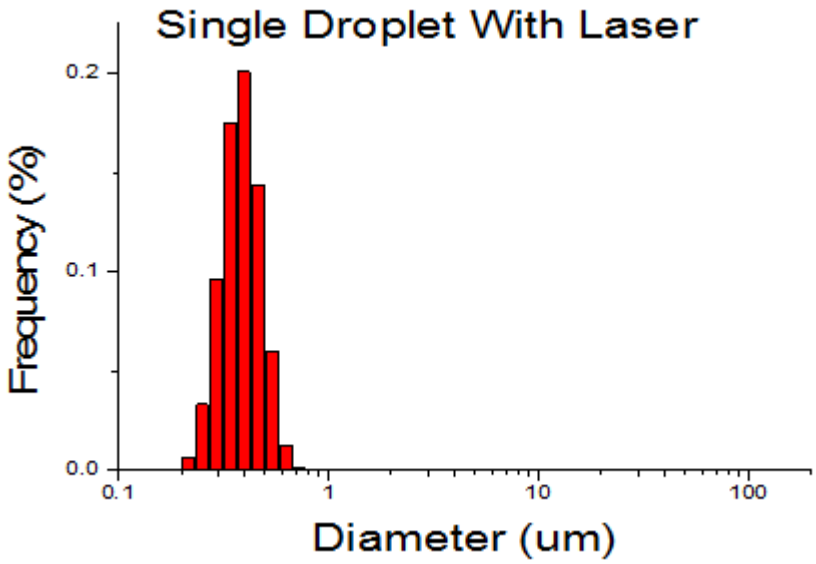

Figure 3.21: Particle size distribution of droplets after the filament-droplet interaction.

A study by Henin *et al.* showed the particle generation of different sizes as the filament interacted with humid air [110]. They have observed three different size ranges that behave differently as they interact with the laser. For the nanoparticles with 25 nm median diameter, the

concentration increases as relative and absolute humidity increases and decreases as the temperature increases. For the particles in the 230-400 nm range the concentration increases with an increase in relative humidity but the concentration decreases as temperature and absolute humidity increases. For the particle with its diameter around 500 nm, the concentration of the particles are no longer dependent on the temperature, relative and absolute humidity.

The observation of the nanoparticles from a single filament interaction with a single droplet is undoubtable. However further studies are required to understand the changes in the size distribution of the nanoparticles due to the surrounding environment for a single filament interaction with a single droplet.

Another experiment was conducted to understand the impact of the filament on concentrated aerosols such as clouds and fogs, the distribution of the particles generated from a large collection of particles interacting with a filament was measured (Figure 3.22). Multiple aerosols with a large peak distribution at 5.64 μm and a variance of 3.05 μm interacted with a single filament. As for the case of a single droplet, sub-micro sized aerosols are created (Figure 3.22 b).

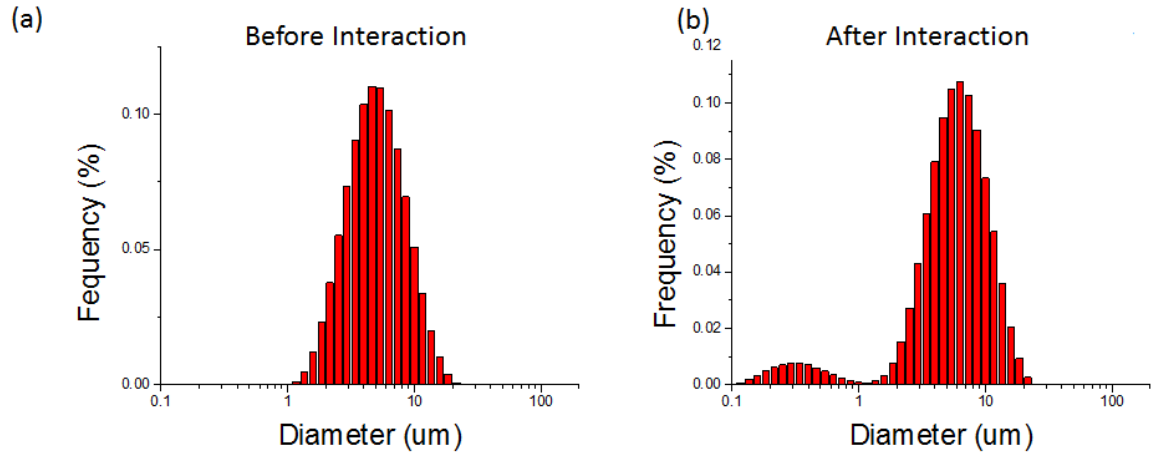

Figure 3.22: Particle size distribution of droplets (a) before and (b) after the filament interaction with multiple aerosols.

These nano-sized particles could coalescence with surrounding aerosols that did not interact with the filament, resulting in the growth of the particle sizes. Several studies focusing on the growth of the particle sizes showed that the photochemical processes from laser-aerosol interaction were important to consider. The laser filament produces O_3 and NO_2 molecules from the ionization of air, which leads to the formation of HNO_3 and then H_2O-HNO_3 nucleation [108, 110].

Further experiments should be conducted to understand the interplay between the fragmentations of the droplets along with the photochemical processes on the growth of the droplets to optimize the laser-induced water condensation in air. In addition to this, the correlation between the growth of the droplet and environmental condition (temperature, pressure, and humidity) should be studied. Nonetheless, the fundamental study of a single

aerosol interaction with a single laser filament mentioned in this chapter is a step towards the complete understanding of filament interaction with multiple aerosols such as clouds and fogs.

4 EFFECT OF PRESSURE ON FILAMENT PROPAGATION

Aerosols are not the only variable that has an impact on filament propagation in the atmosphere. Pressure changes due to the altitude also affect the atmospheric propagation of filaments. In this chapter, the pressure dependence of filament characteristics such as its propagation, intensity profile and supercontinuum generation are discussed.

4.1 Previous Studies

Several studies have been made on filament propagation in adverse conditions such as highly turbulent air [139, 140] or reduced pressures and natural rain in “atmospheric scale” ranges [141]. Multiphoton ionization [142] and blue-shift [143] effects caused by plasma from femtosecond pulses have been studied in low pressure conditions, also called ‘collision-less’ regime ($p << 1atm$). Supercontinuum generation and self-focusing have been investigated experimentally in high-pressure regime ($p > 1$ atm) [54, 144] and it was observed that the threshold for supercontinuum generation and self-focusing decreases as the pressure increases. The pressure independence of some characteristics of filaments such as the clamping of its intensity at the self-focusing distance have been shown [145, 146].

The dependence of start location of the filament on pressure has been studied experimentally and numerically [147, 148]. However, the spatial profile of the filament along propagation has never been the focus of these studies. As it was discussed in Chapter 3, most of the energy of the filament that interacts with the droplet is lost during the filament-droplet interaction. Therefore, by knowing the initial profile of the filament before the interaction, it is

possible to estimate the energy loss of the filament during the filament-aerosol interaction. Thus, the change in the filament beam profile with pressure needs to be understood to account for the energy loss during the interaction.

4.2 Effect of Pressure on Filament Length

To investigate the effect of pressure on the characteristics of the filament propagating in different atmospheric conditions, experiments were conducted with CLaPTAM (Section 2.2) to measure the length, spectrum and the beam profile of the filament at different pressures.

The output of the MTFL (see Section 2.1) with 5 mJ, 50 fs pulses at 800 nm and 10 Hz repetition rate was sent to the CLaPTAM where the pressure was controlled from 76 torr to 760 torr. The total distance between the output of MTFL and the entrance to CLaPTAM was 11 m. The entire pathway of the laser was enclosed with 4 inch pipe tubing to minimize any turbulence as well as for safety reasons.

A 1.2 m focusing lens was placed just prior to the entrance window of CLaPTAM to induce a single filament. Using the grazing incidence beam profiler (see Section 2.2.4), the filament pointing stability was measured out to be ± 200 μm. The plasma emission from the filament was collected from the side using a standard digital SLR camera (Cannon 70D) with 30 second exposure time (i.e. accumulation of 300 single filament images), to measure the filament length (Figure 4.1).

The relationship between the nonlinear index of refraction and pressure is as follows [147]:

$$n_2 = \frac{3\chi^{(3)}}{4\epsilon_o c n_o^2} \times p \qquad (4\text{-}1)$$

where $\chi^{(3)}$ is the third order susceptibility of the medium (esu), ϵ_o is the permittivity of free space (F/m), c is the speed of light (m/s) in vacuum, n_o is the linear refractive index of the medium and p is the pressure in atm.

As the pressure decreases, the nonlinear index of refraction decreases resulting in the increase in the critical power (Equation 1-3). Using Marburger's equation (1-4) it is clear that an increase in the critical power will lead to an increase in the self-focusing distance.

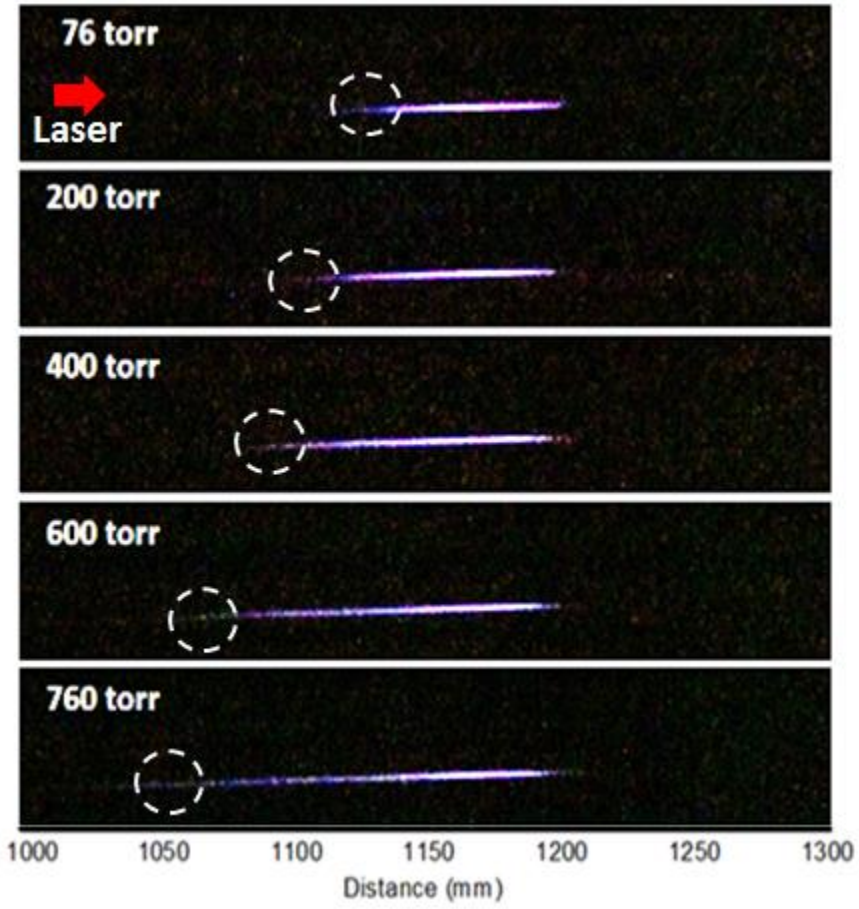

Figure 4.1: Side images of the plasma emission from the filament as the pressure varied from 76 torr to 760 torr. 5 mJ of laser energy with 50 fs pulses at 800 nm was focused with 1.2 m lens.

As it can be seen in Figure 4.1, the collapse location of the filament shifts away from the focusing lens as the pressure is decreased. This shows that as the pressure decreases, the nonlinear index of refraction decreases, resulting in smaller influence of Kerr self-focusing onto the propagating beam. The end location of the filament does not change with respect to the pressure since it is restricted to the external focusing. The divergence of the linear focusing after the focal plane is too strong for the nonlinear effects to overcome.

The beam profile of the filament was measured along propagation at different pressures using the grazing incidence filament beam profiler (see Section 2.2.4)

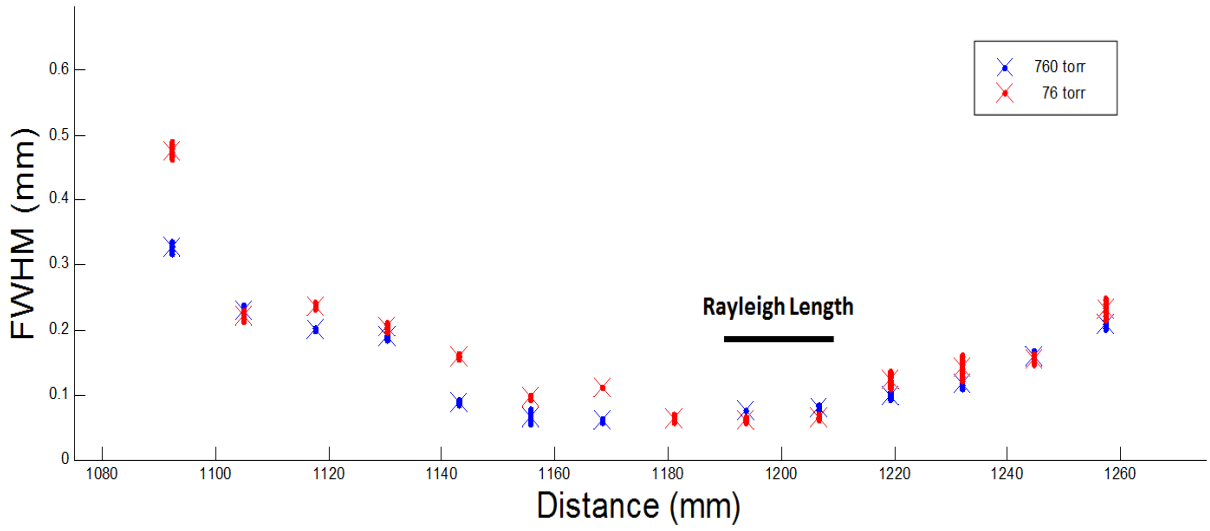

Figure 4.2: Experimental data of the filament diameter at two extreme pressures [76 (red) and 760 (blue) torr] for 1.2 m external focusing.

As it can be seen in Figure 4.2, the beam diameter is less than 0.1 mm for the longitudinal axis from 1150 mm ~ 1210 mm for the 760 torr case while it is less than 0.1 mm from 1180 mm ~ 1210 mm for 76 torr case.

The plasma emission of the filament was also measured for 2.4 m focusing lens (NA = 1.77×10^{-3}) and is shown in Figure 4.3 (b). Similar to the 1.2 m focusing condition, the length of the filament decrease as the pressure decreases from 760 torr to 76 torr.

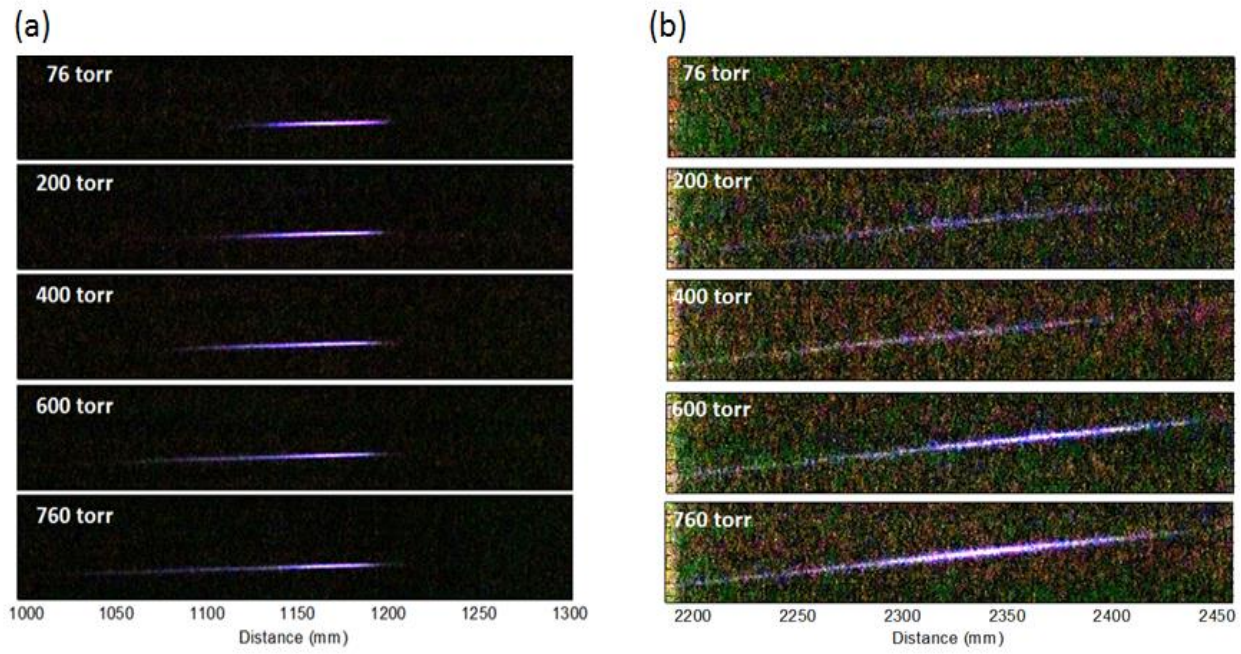

Figure 4.3: Side images of the plasma emission from the filament as the pressure varied from 76 torr to 760 torr for (a) 1.2 m focusing lens (NA = 3.54 x 10^{-3}) (b) 2.4 m focusing lens (NA = 1.77 x 10^{-3})

As discussed previously, the similarity in the increase in the length of the filament can be explained by the Marburger's equation (1-4). The increase in the pressure increases the nonlinear index of refraction resulting in a decrease in the critical power. Therefore, the filament propagating in higher pressure will have an earlier collapse location.

The beam profile measurements of the filament at different pressures were taken using the grazing incidence filament beam profiler (see Section 2.2.4) at various positions along the propagation axis for 2.4 m focusing condition.

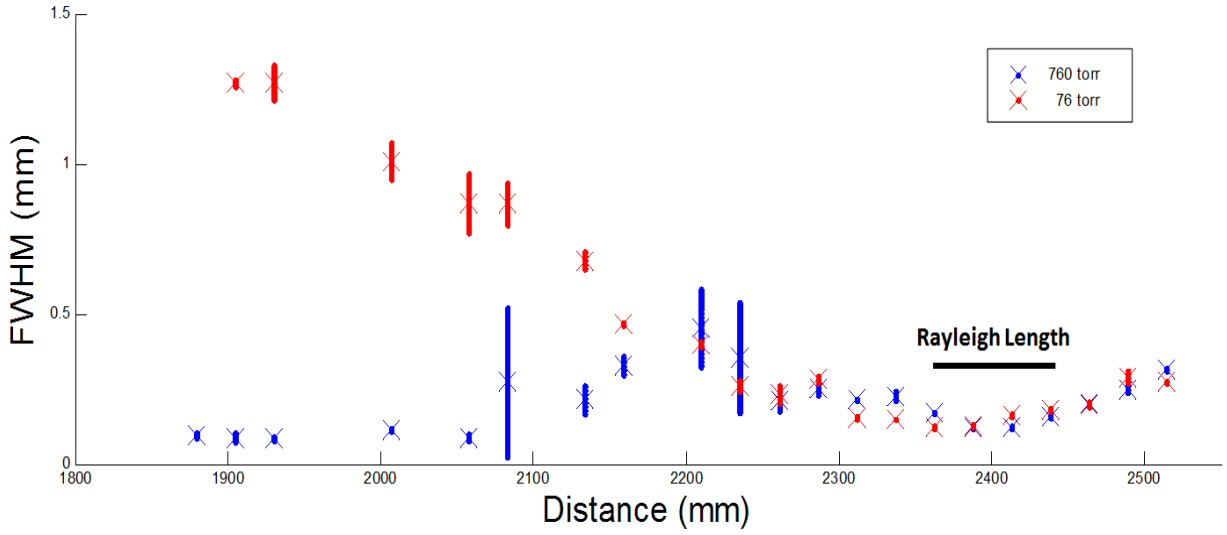

Figure 4.4: Experimental data of the filament diameter at two extreme pressures, 760 torr (blue) and 76 torr (red) for 2.4 m external focusing (NA = 1.77 x 10^{-3})

Compare to the 1.2 m focusing lens (Figure 4.2), a greater changes in filament length and filament beam profile were observed for different pressures. These changes in two different focusing conditions can be explained by the transition from linear-to nonlinear-focusing regime in filamentation. Lim *et al*. studied the characteristic of the filamentation influenced by the numerical aperture used to create the filament [136]. They have shown that depending on the numerical aperture (NA) of the focusing lens, the filament process can be dominated by the geometrical focusing (for high NA) or by the nonlinear process (for low NA). From the experimental data, it is clear that the laser beam with higher NA (1.2 m focusing condition) experiences smaller nonlinear effect compare to the beam with lower NA (2.4 m focusing condition).

4.3 Filament Spectrum at Different Pressures

To further study the transition from geometric focusing regime to the nonlinear focusing regime and to study the impact of pressure on the filament, spectral broadening of the filament using different external focusing conditions (1.2 m, 2.4 m, and 5.8 m) were examined at different pressures. To start with the geometrical focusing regime, a 1.2 m focusing lens was used to induce filamentation in CLaPTAM with laser pulse of 5 mJ, 50 fs pulse width at 800 nm and 10 Hz repetition rate (Figure 4.5).

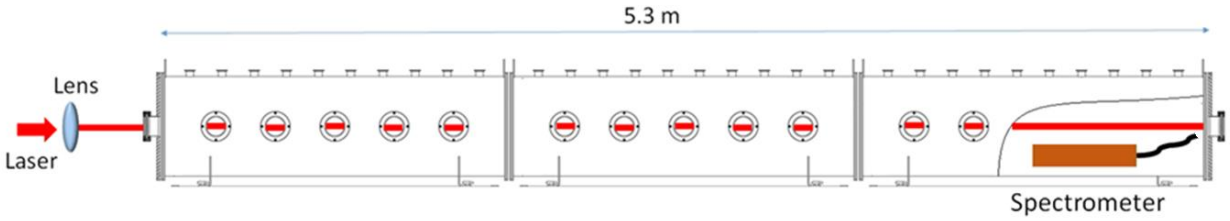

Figure 4.5: Experimental setup for spectral measurement of the filament.

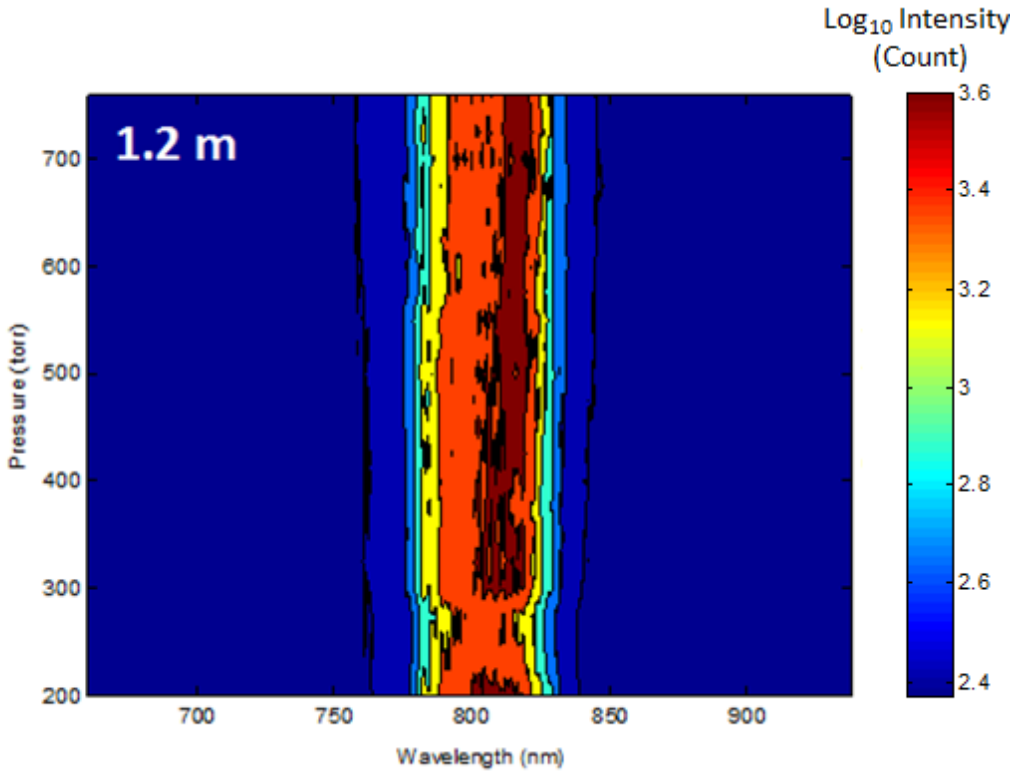

Figure 4.6: Experimental measurement of post filamentation spectrum, for 1.2 m focusing condition, with pressure changing from 200 to 760 torr.

Spectral broadening of the filament was measured as the pressure changed from 200 to 760 torr (Figure 4.6). The spectrum was collected by using Ocean Optics USB 2000 spectrometer with the fiber collecting the scattered light from a target screen located 60 cm after the geometrical focus. As it can be seen from Figure 4.6, the change in spectral broadening is negligible as the pressure is changed. In order to verify the negligible spectral broadening, the spectrum of the filament calculated previously was analyzed for various pressures from 200 to 760 torr.

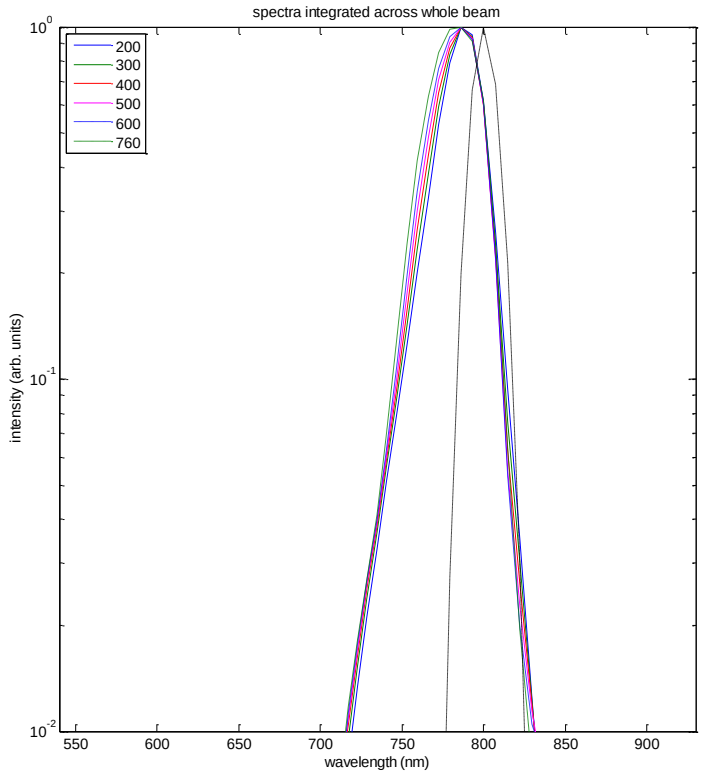

Figure 4.7: Numerical simulation of the spectrum of the filament with 1.2 m focusing lens (NA = 3.54 x 10^{-3}) at different pressures from 200 to 760 torr. Black dashed line shows the initial input spectrum, measured right before the focusing lens.

The simulation results of the spectral broadening for the 1.2 m focusing case (Figure 4.7) shows that the broadening of the spectrum is almost independent of pressure. The agreement between the simulated and experimental data on the independence of spectral broadening on pressure indicates the lack of nonlinearities. Even though the shift in the collapse location revealed the existence of nonlinear self-focusing and its influence on the length of the plasma with respect to the pressure, the nonlinearities was not sufficient enough to change the spectral

characteristics of the beam. Therefore to observed greater changes in the spectral broadening of a filament with respect to the changes in pressure, the initial NA of the beam was decreased to transit into the nonlinear focusing regime. To allow a beam to experience more nonlinearities, slower focusing condition (2.4 m and 5.8 m focal length) were used.

Spectral broadening was measured experimentally for 2.4 m focusing. Unlike the previous results with 1.2 m focusing lens (Figure 4.6), a significant change in spectral broadening was observed for different pressures (Figure 4.8). A slight change ($\Delta\lambda \sim 10$ nm in red) in the broadening was visible for the pressure from 200 - 350 torr. However, there was a significant broadening in both blue and red side of the spectrum above 350 torr, which shows a correlation between the spectral broadening of the filament and the pressure of the medium.

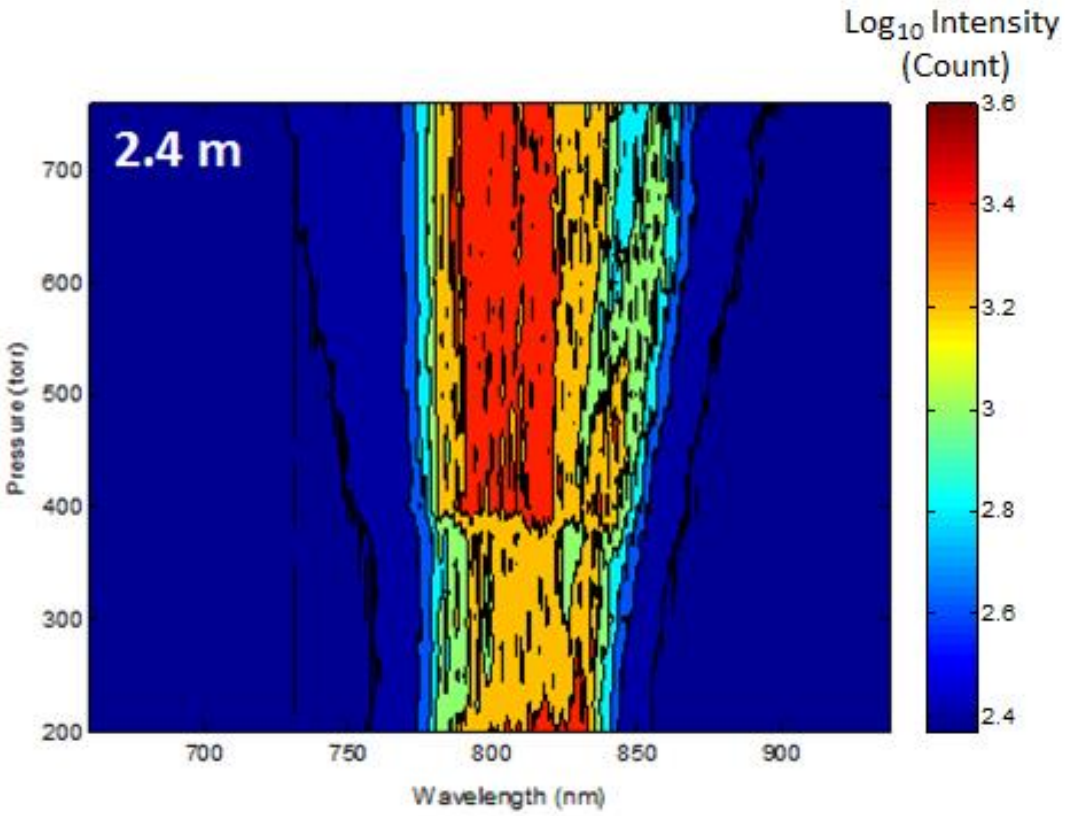

Figure 4.8: Experimental data of spectral broadening of a filament for 2.4 m focusing condition (NA = 1.77 x 10^{-3}) for pressure from 200 to 760 torr.

Figure 4.9 (b) shows the numerical simulations of the spectrum of the filament for 1.2 and 2.4 m focusing conditions. The broadening of the spectrum is highly dependent on the pressure, in the lower NA case (Figure 4.9 b) compare to higher NA case (Figure 4.9 a) which agrees with the experimental data.

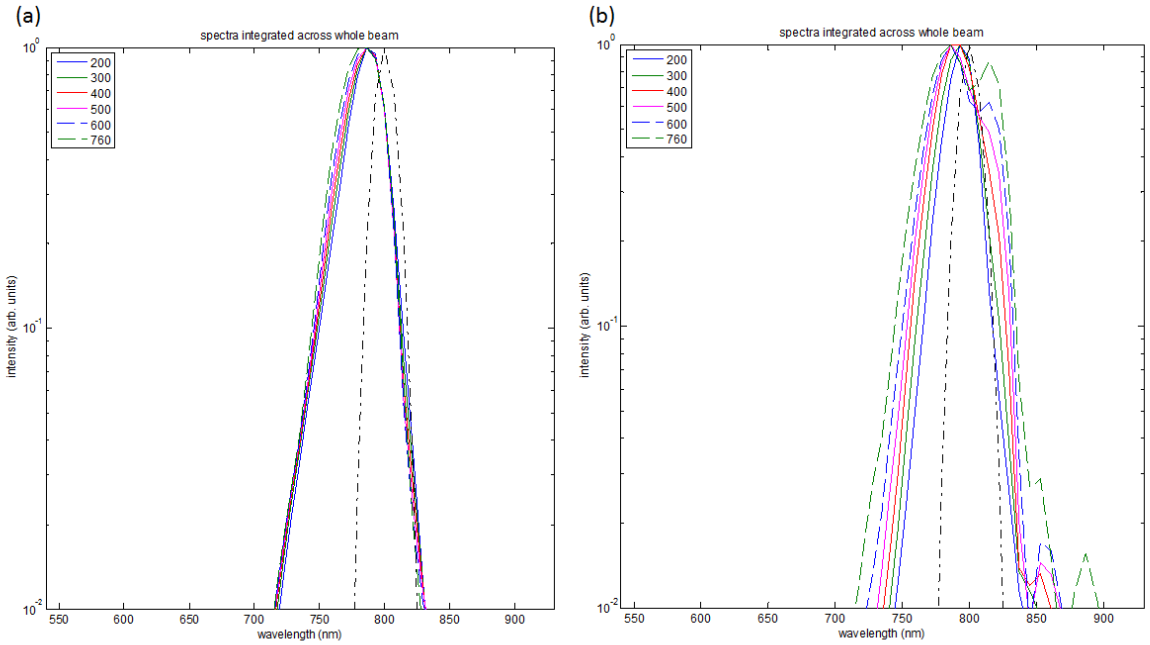

Figure 4.9: Numerical simulation of the spectrum of the filament with (a) 1.2 m focusing lens (NA = 3.54 x 10^{-3}) (b) 2.4 m focusing lens (NA = 1.77 x 10^{-3}) at different pressures from 200 to 760 torr. Black dashed line is the initial input spectrum.

The focal length of the lens was increased to 5.8 m to further study the transition from a geometric focusing regime to nonlinear focusing regime. Since the total length of the chamber is 5.3 m, the 5.8 m focusing lens was positioned 1 m prior to the entrance window of CLaPTAM to allow 5.3 m propagation of the filamenting beam with NA=8.62 x 10^{-4}. Spectral broadening of the filament was measured at the end of CLaPTAM. The spectral broadening for 5.8 m focusing condition at different pressures (Figure 4.10) showed a larger spectral changes than 2.4 m (Figure 4.8) and 1.2 m (Figure 4.6) focusing conditions.

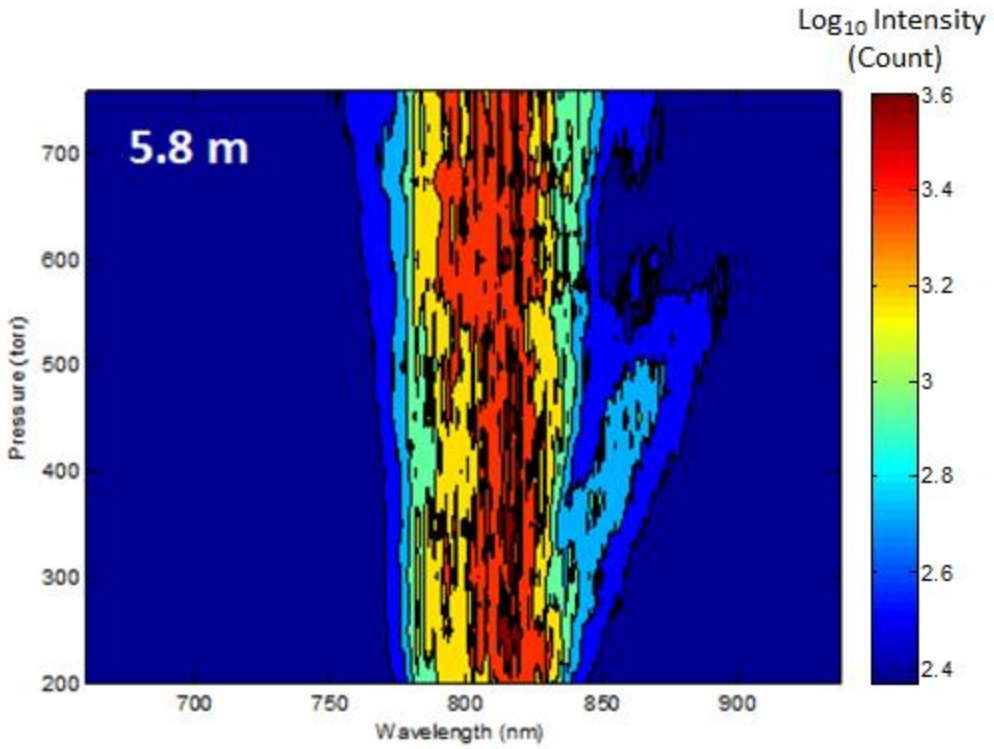

Figure 4.10: Experimental data of spectral broadening of a filament for 5.8 m focusing condition (NA = 8.62 x 10^{-4}) for pressure from 200 to 760 torr.

Unlike the previous results with 2.4 m focusing lens (Figure 4.6), where a significant change in spectral broadening was observed for the pressures 350 torr and above, 5.8 m focusing condition shows a spectral broadening from 200 torr and above (Figure 4.10). This shows that as the NA of the initial beam decreases, where the nonlinear effect dominates filamentation process, the pressure has more influence on the spectral characteristics of the filament.

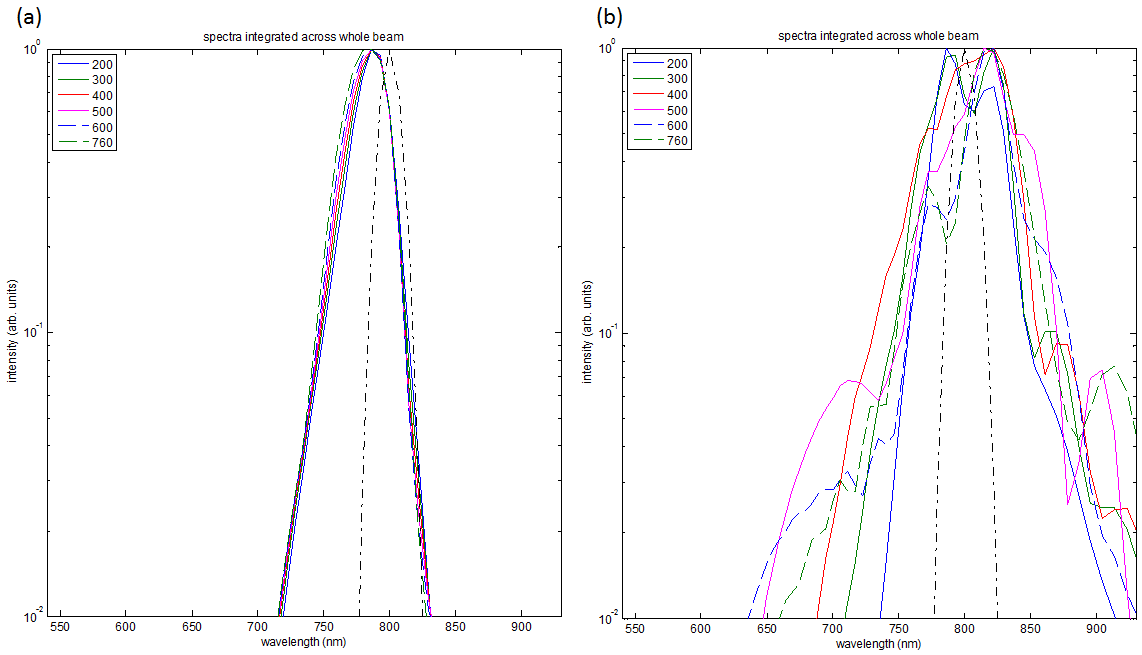

Figure 4.11: Numerical simulation of the spectrum of the filament with (a) 1.2 m focusing lens (NA = 3.54 x 10^{-3}) (b) 5.8 m focusing lens (NA = 8.62 x 10^{-4}) at different pressures from 200 to 760 torr. Black dashed line is the initial input spectrum.

The numerical analysis of the spectral broadening for the 5.8 m focusing condition also showed a significant spectral broadening as the pressure increased (Figure 4.11b). The spectral broadening of the filament at different pressures for various focusing conditions showed that the pressure has greater influence on the spectral characteristic of the filament as NA decreases. Therefore for real world conditions where the filament is formed without any focusing optics (NA = 0), the change in spectral characteristics caused by the pressure changes due to altitude needs to be taken into consideration to perform outdoor filament applications such as LIDAR.

5 CONCLUSION

The ultimate goal for filament applications is to be able to make the transition from the controlled environment of the laboratory to the realistic outdoor conditions. The atmosphere introduces many variables such as humidity, temperature, pressure and aerosols into the equation. These need to be studied individually to completely understand the realistic propagation of filaments. This dissertation focuses on the interaction with the aerosols as well as the influence of pressure on filament propagation.

The robustness of a single filament after interacting with a single aerosol was evaluated. It was shown that even after a significant energy loss (up to 80 %), the filament can resume its propagation. Nonetheless, the relative position of the aerosol to the filament (radially and longitudinally) dictates the reformation of the filament. The formation of the filament can be delayed by interacting with an aerosol during the self-focusing phase. The filament propagation can be interrupted and even be disrupted by an aerosol located farther along the propagation.

The interaction of the water droplets with a single filament leads to their explosion resulting in the generation of nanometric products. When the filament interacts with multiple aerosols, these nanoparticles coalescence with the existing water droplets creating a disturbed cloud distribution.

In order to conduct the controlled study of the mutual influence of the filament on its environment, a high power ultrafast laser and a controllable atmospheric chamber were developed. CLaPTAM (chamber for laser propagation through aerosol medium) has been

designed as part of this work to generate atmospheric conditions similar to several kilometers of altitude by controlling humidity, pressure and temperature.

The effect of pressure on the beam profile along propagation and the supercontinuum generated by the filament was studied. The nonlinear Kerr-effect has a direct dependence on the density of air. Therefore, ultrafast laser pulses propagating at lower pressure experience less Kerr-effect, transitioning towards a linear propagation regime.

The results presented in this dissertation have demonstrated the influence of some of the individual variables that limit filament propagation through atmosphere. The basic principles of filament propagation in different pressures and filament-aerosol interaction are understood. However, the pressure and the aerosols are not the only variables present in filament propagation through atmosphere. Other variables such as temperature, turbulence, and humidity still need to be examined individually. Nonetheless, the development of the CLaPTAM and the preliminary findings in this dissertation are foundations to a complete understanding of filament propagation through atmospheric conditions.

LIST OF REFERENCES

[1] M. Durand, A. Houard, B. Prade, A. Mysyrowicz, A. Durecu, B. Moreau, D. Fleury, O. Vasseur, H. Borchert, K. Diener, R. Schmitt, F. Theberge, M. Chateauneuf, J. Daigle and J. Dubois, "Kilometer range filamentation," *Optics Express,* vol. 21, no. 22, pp. 26836-45, 2013.

[2] G. Mejean, J. Kasparian, E. Slamon, J. Yu, J. Wolf, R. Bourayou, R. Sauerbrey, M. Rodriguez, L. Woste, H. Lehmann, B. Stechklum, U. Laux, J. Elsloffel, A. Scholz and A. Hatzes, "Towards a supercontinuum-based infrared lidar," *Appl. Phys. B,* vol. 77, pp. 357-359, 2003.

[3] R. Chiao, E. Garmire and C. Townes, "Self-trapping of optical beams," *Phys. Rev. Lett,* vol. 13, no. 15, pp. 479-482, 1964.

[4] A. Braun, G. Korn, X. Liu, J. Squier and G. Mourou, "Self-channeling of high-peak-power femtosecond laser pulses in air," *Optics Letters,* vol. 20, no. 1, pp. 73-75, 1 January 1995.

[5] A. Couairon and A. Mysyrowicz, "Femtosecond Filamentation in Transparent Media," *Physics Report,* vol. 441, no. 2-4, pp. 47-189, 2007.

[6] S. Chin, T. Wang and C. Marceau, "Advances in intense femtosecond laser filamentation in air," *Laser Phys.,* vol. 22, no. 1, pp. 1-53, 2011.

[7] S. Chin, Femtosecond Laser Filamentation, Quebec: Springer, 2010.

[8] A. Bandrauk, E. Lorin and J. Moloney, Laser filamentation: Mathmetical methods and models, Springer, 2016.

[9] W. Liu and S. Chin, "Direct measurement of the critical power of femtosecond Ti:sapphire laser pulse in air," *Optics Express,* vol. 13, no. 15, p. 5750, 2005.

[10] Y. Shimoji, A. T. Fay, R. S. F. Chang and N. Djeu, "Direct measurement of the nonlinear refractive index of air," *Journal of the Optical Society of America B,* vol. 6, no. 11, pp. 1997-1998, 1989.

[11] P. Bejot, J. Kasparian and S. Henin, "Higher-Order Kerr Terms Allow Ionization-Free Filamentation in Gases," *Physical Review Letters,* vol. 104, no. 10, p. 103903, 2010.

[12] P. Béjot, E. Hertz, J. Kasparian, B. Lavore, J.-P. Wolf and O. Faucher, "Transition from plasma- to Kerr-driven laser filamentation," *Physics Review Letters,* vol. 106, no. 24, p. 243902, 2011.

[13] Y. E. Geints, A. M. Kabanov, A. A. Zemlyanov, E. E. Bykova and O. A. Bukin, "Kerr-driven nonlinear refractive index of air at 800 and 400nm measured through femtosecond laser pulse filamentation," *Applied Physics Letters,* vol. 99, no. 18, p. 181114, 2011.

[14] K. D. Moll and A. L. Gaeta, "Self-Similar Optical Wave Collapse: Observation of the Townes Profile," *Physical Review Letters,* vol. 90, no. 20, p. 203902, 2003.

[15] R. Y. Chiao, E. Garmire and C. H. Townes, "Self-Trapping of Optical Beams," *Physical Review Letters,* vol. 13, no. 15, pp. 479-482, 1964.

[16] J. H. Marburger, "Self-focusing: theory," *Progress in Quantum Electronics,* vol. 4, pp. 35-110, 1975.

[17] G. Fibich and A. L. Gaeta, "Critical power for self-focusing in bulk media and in hollow waveguides," *Optics Letters,* vol. 25, no. 5, pp. 335-337, 2000.

[18] J. Kasparian, R. Sauerbrey and S. Chin, "The critical laser intensity of self-guided light filaments in air," *Applied Physics B,* vol. 71, no. 6, pp. 877-879, 2000.

[19] V. Talanov, "Focusing of light in cubic media," *Journal of Experimental and Theoretical Physics Letters,* vol. 11, no. 6, pp. 199-201, 1970.

[20] A. Kudrin and V. Krainov, "Tunneling ionization of a hydrogen molecule by a static electric field," *Laser Physics,* vol. 13, no. 8, pp. 1024-1029, 2003.

[21] S. Chin and P. Lambropoulos, Multiphoton ionization of atoms, Academic Press, 1984.

[22] N. Belone and V. Krainov, Multiphoton processes in atoms, Springer, 2000.

[23] L. Lompre, A. L'Huillier and G. Mainfray, "Laser-intensity effects in the energy distribution of electrons produced in multiphoton ionization of rare gases," *J. Opt. Soc. Am. B,* vol. 2, no. 12, pp. 1906-1912, 1985.

[24] C. Guo, M. Li, J. Nibarger and G. Gibson, "Single and double ionization of diatomic molecules in strong laser fields," *Physical Review A,* vol. 58, no. 6, p. 4271, 1998.

[25] R. Kulygin and V. Taranukhin, "Tunneling ionization of atoms and ions in a strong laser field and the effect of local ionization suppression," *laser Physics,* vol. 3, no. 3, pp. 644-650, 1993.

[26] X. Tong, Z. Zhao and C. Lin, "Theory of molecular tunneling ionization," *Phys. Review A,* vol. 66, p. 033402, 2002.

[27] L. Keldysh, "Ionization in the field of a strong electromagnetic wave," *Soviet Physics JETP,* vol. 20, no. 5, pp. 1307-1314, 1965.

[28] V. Popov, "Tunnel and multiphoton ionization of atoms and ions in a strong laser filed (Keldysh theory)," *UFN,* vol. 174, no. 9, pp. 921-951, 2004.

[29] G. Zhan, J. Nichols and D. Dixon, "Ionization potoential, electron affinity, electronegativity, hardness, and electron excitation energy: molecular properties from density functional theory orbital energies," *J. Phys. Chem A,* vol. 107, p. 4184, 2003.

[30] M. Feit and J. Fleck, "Effect of refraction on spot-size dependence of laser-induced breakdown," *Appl. Phys. Lett,* vol. 24, p. 169, 1974.

[31] M. Kilesik, E. Wright and J. Moloney, "Femtosecond filamentation in air and higher-order nonlinearities," *Optics Letters,* vol. 35, no. 15, p. 2550, 2010.

[32] Y. Chen, S. Varma, T. Antonsen and H. Milchberg, "Direct measurement of the electron density of extended femtosecond laser pulse-induced filaments," *Physical Review Letters,* vol. 105, p. 215005, 2010.

[33] C. Bree, A. Demircan and G. Steinmeyer, "Saturation of the all-optical kerr effect," *Physical review letters,* vol. 106, p. 183902, 2011.

[34] V. Loriot, E. Hertz, O. Faucher and B. Lavorel, "Measurement of high order Kerr refractive index of major air components: erratum," *Optics Express,* vol. 18, no. 3, p. 3011, 2010.

[35] M. Mlejnek, E. Wright and J. Moloney, "Dynamic spatial replenishment of femtosecond pulses propagatin gin air," *Optics Letters,* vol. 23, no. 5, p. 382, 1998.

[36] F. Théberge, W. Liu, P. Simard, A. Becker and S. Chin, "Plasma density inside a femtosecond laser filament in air: Strong dependence on external focusing," *Physical Review E,* vol. 74, p. 36406, 2006.

[37] Y. Chen S. Varma, T. M. Antonsen, and H. M. Milchberg, "Direct measurement of electron density of extended femtosecond llaser pulse-induced filaments," *Physical Review Letters,* vol. 105, p. 215005, 2010.

[38] H. Schillinger and R. Sauerbrey, "Electrical conductivity of long plasma channels in air generated by self-guided femtosecond laser pulses," *Appl. Phys. B,* vol. 68, no. 4, pp. 753-756, 1999.

[39] H. Yang, J. Zhang, Y. Li, J. Zhang, Y. Li, Z. Chen, H. Teng, Z. Wei and Z. Sheng, "Characteristics of self-guided laser plasma channels generated by femtosecond laser pulses in air," *Phys. Rev. E,* vol. 66, p. 016406, 2002.

[40] J. Papeer, M. Botton, D. Gordon, P. Sprangle, A. Zigler and Z. Henis, "Extended lifetime of high density plasma filament generated by a dual femtosecond-nanosecond laser pulse in air," *New Journal of Physics,* vol. 16, p. 123046, 2014.

[41] S. Tzortzakis, B. Prade, M. Fanco and A. Mysyrowicz, "Time-evolution of the plasma channel at the trail of a self guided IR femtosecond laser pulse in air," *Optics Communications,* vol. 181, no. 1-3, pp. 123-127, 2000.

[42] S. Bodrov, V. Bukin, M. Tsarev, A. Murzanev, S. Garnov, N. Aleksandrov and A. Stepanov, "Plasma filmanet investigation by transverse optical interferometry and terahertz scattering," *Optics Express,* vol. 19, no. 7, p. 6829, 2011.

[43] J. Wahlstrand, Y. Chen, Y. Cheng, S. Varma and H. Milchberg, "Measurement of the high field optical nonlinearity and electron density in gases: application to filamentation experiments," *IEEE Journal of Quantum Electronics,* vol. 48, no. 6, p. 760, 2012.

[44] V. Kandidov, V. Fedorov, O. Tverskoy, O. Kossareva and S. Chin, "Intensity clamping in the filament of femtosecond laser radiation," *Quantum Electronics,* vol. 41, no. 4, p. 382, 2011.

[45] A. Brodeur, C. Chien, F. Ilkov and S. Chin, "Moving focus in the propagation of ultrashort laser pulses in air," *Potics Letters,* vol. 22, no. 5, pp. 304-306, 1997.

[46] E. Nibbering, P. Curley, G. Grillon, B. Prade, M. Franco, F. Salin and A. Mysyrowicz, "Conical emission from self-guided femtosecond pulses in air," *Optics Letters,* vol. 21, no. 1, pp. 62-64, 1996.

[47] O. Kosareava, V. Kandidov, A. Brodeur, C. Chien and S. Chin, "Conical emission from laser-plasma interactions in the filamentation of powerful ultrashort laser pulses in air," *Optics Letters,* vol. 22, no. 17, pp. 1332-1334, 1997.

[48] W. Liu, F. Théberge, J.-F. Gravel, A. Becker and S. L. Chin, "Experiment and simulations on the energy reservoir effect in femtosecond light filaments," *OPTICS LETTERS,* vol. 30, no. 19, pp. 2602-2604, 2005.

[49] F. Courvoisier, V. Boutou, J. Kasparian, E. Salmon, G. Y. J. Méjean and J. Wolf, "Ultraintense light filaments transmitted through clouds," *Applied Physics Letters,* vol. 83, no. 2, pp. 213-215, 2003.

[50] M. Kolesik and J. V. Moloney, "Self-healing femtosecond light filaments," *Optics Letters,* vol. 29, no. 6, pp. 590-592, 2004.

[51] A. Dubietis, E. Kucinskas, G. Tamosauskas and E. Gaizauskas, "Self-reconstruction of light filaments," *Optics Letters,* vol. 29, pp. 2893-2895, 2004.

[52] S. Eisenmann, J. Penano, P. Sprangle and A. Zigler, "Effect of an energy reservoir on the atmospheric propagation of laser-plasma filaments," *Physical Review Letters,* vol. 100, p. 155003, 2008.

[53] V. Kandidov, O. Kosareva and I. Golubtsov, "Self-transformation of a powerful femtosecond laser pulse into a white-light laser pulse in bulk optical media (or supercontinuum generation)," *Applied Physics B,* vol. 77, pp. 149-165, 2003.

[54] P. Corkum, C. Rolland and T. Srinivasan-Rao, "Supercontinuum Generation in Gases," *Physical Review Letters,* vol. 57, no. 18, pp. 2268-2271, 1986.

[55] S. Uhlig, Self-Organized Surface Structures with Ultrafast White-Light, Springer, 2015.

[56] M. Weidman and M. Richardson, "Laser filamentation interaction with materials for spectroscopic applications," PhD Dissertation, CREOL, The College of Optics and Photonics, Orlando, 2012.

[57] M. Durand, K. Lim, V. Junkna, E. McKee, M. Baudelet, A. Houard, M. Rochardson, A. Mysyrowicz and A. Couairon, "Blueshifted continuum peaks from filamentation in the anomalous dispersion regime," *Physical Review A,* vol. 87, p. 043820, 2013.

[58] S. Rostami, M. Chini, K. Lim, J. Palastro, M. Durand, J. Diels, L. Arissian, M. Baudelet and M. Richardson, "Dramatic enchancement of supercontinuum generation in elliptically-polarized laser filaments," *Scientific Reports,* vol. 6, p. 20363, 2016.

[59] T. Xi, Z. Zhao and Z. Hao, "Filamentation of femtosecond laser pulses with spatial chirp in air," *J. Opt. Soc. Am. B,* vol. 31, no. 2, p. 321, 2014.

[60] R. Ensley, D. Fishman, S. Webster, L. Padilha, D. Hagan and E. Van Stryland, "Energy and spectral enhancement of femtosecond supercontinuum in a noble gas using a weak seed," *Optics Express,* vol. 19, no. 2, p. 757, 2011.

[61] M. K. M. Thomson, T. Loffler and H. Roskos, "Broadband THz emission from gas plasmas induced by femtosecond optical pulses: From fundamentals to applicaions," *Laser & Photon. Rev.,* vol. 1, no. 4, p. 349, 2007.

[62] P. Sprangle, J. Penano, B. Hafizi and C. Kapetanakos, "Ultrashort laser pulses and electromagnetic pulse generation in air and on dielectric surfaces," *Physical Review E,* vol. 69, p. 066415, 2004.

[63] H. Hamster, A. Sullivan, S. Gordon and R. Falcone, "Short-pulse terahertz radiation from high-intensity-laser-produced plasmas," *Physical Reeview E,* vol. 49, no. 1, p. 671, 1994.

[64] R. Bernath and M. Richardson, "High-intensity ultra-fast laser interaction technologies," PhD Dissertation, CREOL, The College of Optics and Photonics, Orlando, 2006.

[65] F. Courvoisier, V. Boutou, J. Kasparian, E. Salmon, G. Mejean, J. Yu and J. Wolf, "Ultraintense light filaments transmitted through clouds," *Applied Physics Letters,* vol. 83, no. 2, pp. 213-215, 2003.

[66] S. Skupin, L. Berge, U. Peschel and F. Lederer, "Interaction of Femtosecond Light Filaments with Obscurants in Aerosols," *Physical Review Letters,* vol. 93, no. 2, p. 023901, 2004.

[67] G. Méchain, G. Méjean, R. Ackermann, P. Rohwetter, Y.-B. André, J. Kasparian, B. Prade, K. Stelmaszczyk, J. Yu, E. Salmon, W. S. Winn, A. Mysyrowicz, R. Sauerbrey, L. Wöste and J.-P. Wolf, "Propagation of fs-TW laser filaments in adverse atmospheric conditions," *Appl.Phys.B,* vol. 80, pp. 785-789, 2005.

[68] H. L. Xu and S. L. Chin, "Femtosecond Laser Filamentation for Atmospheric Sensing," *Sensors,* vol. 11, no. 1, pp. 32-53, 2011.

[69] A. Miziolek, V. Palleschi and I. Schechter, Laser induced breakdown spectroscopy: Fundamentals and Applications, Cambridge University Press, 2006.

[70] S. Tzortzakis, D. Anglos and D. Gray, "Ultraviolet laser filaments for remote laser-induced breakdown spectroscopy (LIBS) analysis: applications in cultural heritage monitoring," *Opt. Lett.,* vol. 31, no. 8, p. 1139, 2006.

[71] M. Weidman, M. Baudelet, M. Fisher, C. Bridge, B. C., M. Sigman, P. Dagdigian and M. Richardson, "Molecular signal as a signature for detection of energetic materials in filament-induced breakdown spectroscopy," in *SPIE Proceedings Vol.7304,* 2009.

[72] P. Rohwetter, J. Yu, G. Mejean, K. Stelmaszczyk, E. Salmon, J. Kasparian, J. Wolf and L. Woste, "Remote LIBS with ultrashort pulses: characteristics in picosecond and femtosecond regimes," *J. Anal. At. Spectrom.,* vol. 19, p. 437, 2004.

[73] P. S. K. Rohwetter, L. Woste, R. Ackermann, G. Mejean, E. Slamon, J. Kasparian, J. Yu and J. Wolf, "Fialment-induced remote surface ablation for long range laser induced breakdown spectrocsopy operation," *Spectrochimica Acta Part B: Atomic Spectroscopy,* vol. 60, no. 7-8, p. 1025, 2005.

[74] M. Baudelet, L. Guyon, J. Yu, J. A. T. Wolf, E. Frejafon and P. Laloi, "Femtosecond time-resolved laser-induced breakdown spectroscopy for detection and identification of bacteria: A comparison to the nanosecond regime," *Journal of Applied Physics,* vol. 99, p. 084701, 2006.

[75] K. Stelmaszczyk, P. Rohwetter, G. Mejean, J. Yu, E. Salmon, J. Kasparian, R. Ackermann and J. Wolf, "Long-distance remote laser-induced breakdown spectroscopy using filamentation in air," *Applied Physics Letters,* vol. 85, no. 18, p. 3977, 2004.

[76] T. Labutin, V. Lednev, A. Ilyin and A. Popov, "Femtosecond laser-induced breakdown spectroscopy," *Journal of analytical atomic spectrometry,* vol. 31, p. 90, 2016.

[77] J. Kasparian, M. Rodriguez, G. Mejean, J. Yu, E. Salmon, H. Wille, R. Bourayou, S. Frey, Y. Andre, A. Mysyrowicz, R. Sauerbrey, J. Wolf and L. Woste, "White-Light Filaments for Atmospheric Analysis," *Science,* vol. 301, no. 5629, p. 61, 2003.

[78] R. Bourayou, G. Mejean, G. Kasparian, M. Rodriguez, E. Slamon, J. Yu, H. S. B. Lehmann, U. Lauz, J. Eisloffel, A. Scholz, A. Hatzes, R. Sauerbrey, L. Woste and J. Wolf, "White-light filaments for multiparameter analysis of cloud microphysics," *J. Opt. Soc. Am. B,* vol. 22, no. 2, p. 369, 2005.

[79] J. Kasparian, R. Sauerbrey, D. Mondelain, S. Niedermeier, J. Yu, J. WOlf, Y. Andre, M. Franco, B. Prade, S. Tzortzakis, A. Mysyrowicz, M. Modriguez, H. Wille and L. Woste, "Infrared extension of the super continuum generated by femtosecond terawatt laser pulses propagating in the atmosphere," *Optics Letters,* vol. 25, p. 1397, 2000.

[80] L. Berge, S. Skupin, G. Mejean, J. Kasparina, J. Yu, S. Frey, E. Salmon and J. Wolf, "Supercontinuum emission and enhanced self-guiding of infrared femtosecond filaments sustained by third-harmonic generation in air," *Physical Review E,* vol. 71, p. 016602, 2005.

[81] J. Yu, D. Mondelain, G. Ange, R. Volk, S. Niedermeier and J. Wolf, "Backward supercontinuum emission from a filament generated by ultrashort laser pulsees in air," *Optics Letters,* vol. 26, no. 8, p. 533, 2001.

[82] P. Rairoux, H. Schillinger, M. Niedermeier, F. Ronneberger, R. Sauerbrey, B. Stein, D. Waite, C. Wedekind, H. Wille, L. Woste and C. Ziener, "Remote sensing of the atmosphere using ultrashort laser pulses," *Appl. Phys. B,* vol. 71, p. 573, 2000.

[83] M. Petrarca, S. Henin, N. Berti, M. Matthews, J. Chagas, J. Kasparian, W. J.P., G. Gatti, G. Pirro, M. Anania, M. Ferrario and A. Ghigo, "White-light femtosecond lidar at 100 TW power level," *Appl. Phys. B,* vol. 114, p. 319, 2014.

[84] V. Blank, M. Thomson and H. Roskos, "Spatio-spectral characteristics of ultra-broadband THz emission from two-colour photoexcited gas plasmas and their impact for nonlinear spectroscopy," *New J. Phys.,* vol. 15, p. 075023, 2013.

[85] A. Houard, Y. Liu, B. Prade, V. T. Tikhonchuk and A. Mysyrowicz, "Strong Enhancement of Terahertz Radiation from Laser Filaments in Air by a Static Electric Field," *Physical Review Letters,* vol. 100, p. 255006, 2008.

[86] N. Karpowicz, X. Lu and X.-C. Zhang, "Terahertz gas photonics," *Journal of Modern Optics,* vol. 56, no. 10, p. 1137, 2009.

[87] Y. Chen, H. Liu, Y. Deng, D. Schauki, M. J. Fitch, R. Osiander, C. Dodson, J. Spicer, M. Shur and X. –C, Zhang, "THz Spectroscopic Investigation of 2,4-Dinitrotoluene," *Chem. Phys. Lett.,* vol. 400, p. 357, 2004.

[88] Y. Chen, H. Liu, Y. Deng, D. Veksler, M. Shur and X. –C. Zhang, "Spectroscopic Characterization of Explosives in the Far Infrared Region," *THz for Military and Security Applications II, Proc. SPIE,* vol. 5411, pp. 1-8, 2004.

[89] M. J. Fitch, D. Schauki, C. A. Kelly and R. Osiander, "THz Imaging and Spectroscopy for Landmine Detection," *in THz and Gigahertz z Electronics and Photonics III, Proc. SPIE ,* vol. 5354, p. 45, 2004.

[90] V. Valuev, A. Dormidonov, V. Kandidov, S. Shlenov, V. Kornienko and V. Cherepenin, "Plasma channels formed by a set of filaments as a guiding system for microwave radiation," *Journal of Communications Technology and Electronics,* vol. 55, no. 2, pp. 208-214, 2010.

[91] N. Barbieri, "Engineering and application of ultrafast laser pulses and filamentation in air," University of Central Florida, Orlando, 2012.

[92] M. Chateauneuf, S. Payeur, J. Dubois and J. Kieffer, "Microwave guiding in air by a cylindrical filament array waveguide," *Applied Physics Letters,* vol. 92, p. 091104, 2008.

[93] Z. Kudyshev, R. M. and N. Litchinitser, "Virtual hyperbolic metamaterials for manipulating radar signals in air," *Nature Communications,* vol. 4, p. 2557, 2013.

[94] J. Kasparian, R. Ackermann, Y. Andre, G. Mechain, G. Mejean, P. B., P. Rohwetter, E. Salmon, K. Stelaszczyk, J. Yu, A. Mysyrowicz, R. Sauerbrey, L. Woste and J. Wolf, "Electric events synchronized with laser filaments in thunderclouds," *Optics Express,* vol. 16, no. 8, p. 5757, 2008.

[95] M. Henriksson, J. Daigle, F. Theberge, M. Chateauneuf and J. Dubois, "Laser guiding of Tesla coil high volatage discharges," *Optics Express,* vol. 20, no. 12, p. 12721, 2012.

[96] Z. Zhang, X. Lu, W. Liang, Z. Hao, M. Zhou, Z. Wang, X. Liu and J. Zhang, "Triggering and guiding HV discharge in air by filamentation of single and dual fs pulses," *Optics Express,* vol. 17, no. 5, p. 3461, 2009.

[97] X. Zhao, J. Diels, C. Wang and J. Elizondo, "Femtosecond ultraviolet laser pulse induced lighning discharges in gases," *IEEE journal of Quantum Electronics,* vol. 31, no. 3, pp. 599-612, 1995.

[98] J. Kasparian and J. Wolf, "On lightning control using lasers," in *Progress in ultrafast intense laser science V,* vol. 98, Springer, 2010, pp. 109-122.

[99] S. Henin, K. Stelmaszczyk, M. Petrarca, P. Rohwetter, Z. Hao, J. Luder, Y. Petit, A. Vogel, K. Weber, J. Kasparian, L. Woste and J. Wolf, "Laser filament induced water condensation," *EPJ Web of Conferences,* vol. 41, p. 12008, 2013.

[100] J. Kasparian, P. Rohwetter, L. Woste and A.-P. Wolf, "Laser-assisted water condensation in the atmosphere: a step towards modulating precipitation," *Journal of Physics D: Applied Physics,* vol. 45, p. 293001, 2012.

[101] H. Sun, J. Liu, C. Wang, J. Ju, Z. Wang, W. Wang, X. Ge, C. Li, S. Chin, R. Li and Z. Xu, "laser filamentation induced air-flow motion in a diffusion cloud chamber," *Optics Express,* vol. 21, no. 7, pp. 9255-9266, 2013.

[102] H. Saathoff, S. Henin, K. Stelmaszczyk, M. Petrarca, R. Delagrange, Z. Hao, J. Luder, O. Mohler, Y. Petit, P. Rohwetter, M. Schnaiter, J. Kasparian, T. Leisner, J. Wolf and L. Woste, "Laser filament-induced aerosol formation," *Atmos. Chem. Phys.,* vol. 13, pp. 4593-4604, 2013.

[103] A. Lindinger, J. Hagen, L. Socaciu, T. Bernhardt, L. Woste, D. Duft and T. Leisner, "Time-resolved explosion dynamics of H2O droplets induced by femtosecondn laser pulses," *Applied Optics,* vol. 43, no. 27, pp. 5263-5269, 2004.

[104] E. Efimenko, Y. malkov, A. Murzanev and A. Stepanov, "Femtosecond laser pulse-induced breakdown of a single water microdroplet," *J. Opt. Soc. Am. B,* vol. 31, no. 3, pp. 534-541, 2014.

[105] J. Feichter and T. Leisner, "Climate engineering: A critical review of approaches to modify the global energy balance," *The European Physical Journal Special Topics,* vol. 176, pp. 81-92, 2009.

[106] J. Ju, J. Sun, A. Sridharan, T. Wang, C. Wang, J. Liu, R. Li, Z. Xu and S. Chin, "Laser-filament-induced snow formation in a subsaturated zone in a cloud chamber: Experimental and theoretical study," *Physical Review E,* vol. 88, p. 062803, 2013.

[107] H. Liang, H. Sun, Y. Liu, Y. Tian, J. Ju, C. Wang and J. Liu, "Chirp control of femtosecond laser-filamentation-induced snow formation in a cloud chamber," *Chinese Optics Letters,* vol. 13, no. 3, p. 033201, 2015.

[108] P. K. J. Rohwetter, K. Stelmaszczyk, Z. Hao, S. Henin, N. Lascoux, W. Nakaema, Y. Petit, M. Quisser, R. Salame, E. Salmon, L. Woste and J. Wolf, "Laser-induced water condensation in air," *Nature Photonics,* vol. v, p. 451, 2010.

[109] Y. Petit, S. Henin, J. Kasparian, J. Wolf, P. Rohwetter, K. Stelmaszczyk, Z. Hao, W. Nakaema, L. Woste, A. Vogel, T. Pohl and K. Weber, "Influence of pulse duration, energy, and focusing on laser-assisted water condensation," *Applied Physics Letters,* vol. 98, p. 041105, 2011.

[110] S. Henin, Y. Petit, P. Rohwetter, K. Stelmaszczyk, Z. Hao, W. Nakaema, A. Volgel, T. Pohl, F. Schneider, J. Kasparian, K. Weber, L. Woste and J. Wolf, "Field measurements suggest the mechanism of laser-assisted water condensation," *Nature Communications,* vol. 2, p. 456, 2011.

[111] J. Ju, J. Liu, C. Wang, H. Sun, W. Wang, X. Ge, C. Li, S. Chin, R. Li and Z. Xu, "Laser-filamentation-induced condensation and snow formation in a cloud chamber," *Optics Letters,* vol. 37, no. 7, p. 1214, 2012.

[112] J. Ju, T. Leisner, H. Sun, A. Sridharan, T. Wang, J. Wang, C. Wang, J. Liu, R. Li, Z. Xu and S. Chin, "Laser-induced supersaturation and snow formation in a sub-satuarated cloud chamber," *Appl. .Phys. B,* vol. 117, p. 1001, 2014.

[113] T. Leisner, D. Duft, O. Möhler, H. Saathoff, M. Schnaiter, S. Henin, K. Stelmaszczyk, M. Petrarca, R. Delagrange, Z. Hao, J. Lüder, Y. Petit, P. Rohwetter, J. Kasparian, J. Wolf and L. Wöste, "Laser-induced plasma cloud interaction and ice multiplication under cirrus cloud conditions," *Proc. Natl. Acad. Sci. U. S. A.,* vol. 110, no. 25, p. 10106, 2013.

[114] K. Lim and M. Richardson, "Laser filamentation-beyond self-focusing and plasma defocusing," PhD Dissertation, CREOL, The College of Optics and Photonics, Orlando, 2014.

[115] W. Hsieh, "Representing droplet size distribution and cloud processes in aerosol-cloud-climate interaction studies," Georgia Institute of Technology, 2007.

[116] R. Kapoor, S. Paul, A. Ramachandra Murty, K. Krishna, S. Sharma and B. Ramana Murty, "Measurement of cloud droplet size distribution in seeded warm cumulus clouds," *Pageoph,* vol. 114, 1946.

[117] S. Henin, "Laser filament-induced aerosol generation in the atmosphere," UNIVERSITE DE GENEVE, 2013.

[118] R. Wagner, C. Linke, K. Naumann, M. Schnaiter, M. Vragel, M. Gangl and H. Horvath, "A review of optical measurements at the aerosol and cloud chamber AIDA," *Journal of Quantitative Spectroscopy & Radiative Transfer,* vol. 110, pp. 930-949, 2009.

[119] G. Méjean, J. Kasparian, J. Yu, E. Salmon, S. Frey and J.-P. Wolf, "Multifilamentation transmission through fog," *Physical Review E,* vol. 72, no. 2, p. 026611, 2005.

[120] W. Liu, O. Kosareva, I. Golubtsov, A. Iwasaki, A. Becker, V. Kandidov and S. Chin, "Random deflection of the white light beam during self-focusing and filamentation of a femtosecond laser pulse in water," *Applied Physics B,* vol. 75, pp. 595-599, 2002.

[121] Y. Geints, A. Zemlyanov, A. Kabanov, E. Bykoya, D. Apeksimov, O. Bulkin, E. Sokolova, S. Golik and A. Liyin, "Angular diagram of broadband emissio nof millimeter-sized water dropelts exposed to gigawatt femtosecond laser pulses," *Appl. Opt.,* vol. 50, no. 27, pp. 5291-5298, 2011.

[122] C. Jeon, D. harper, K. Lim, M. Durnad, C. M., M. Baudelt and M. Richardson, "Interaction of a single filament witha single water droplet," *Jornal of Optics,* vol. 17, p. 055502, 2015.

[123] Y. Zel'dovich and Y. Raizer, Physics of shcok waves and high-temperature hydrodynamic phenomena, Mineola: Dover Publications, 2002.

[124] S. Harilal, G. Miloshevsky, P. Diwakar, N. LaHaye and Hassanein, "Experimental and computational study of complex schowave dynamics in laser ablation plumes in argon atmosphere," *Physics of Plasmas,* vol. 19, p. 083504, 2012.

[125] A. Miloshevsky, S. Harilal, G. Miloshevsky and A. Hassanein, "Dynamics of plasma expansion and shockwave formation in femtosecond laser-ablated aluminum plumes in argon gas at atmospheric pressures," *Physics of Plasmas,* vol. 21, p. 043111, 2014.

[126] F. Potemin, E. Mareev, A. Podshivalov and V. Gordienko, "Laser Control of filament-induced shockwave in water," *Laser Phys. Lett.,* vol. 11, p. 106001, 2014.

[127] B. Bernath, C. Brown, J. Aspiotis, M. Fisher and M. Richardson, "Shock-wave generation in transparent media from ultra-fast lasers," *Proc. of SPIE,* vol. 6219, p. 62190A, 2006.

[128] J. Yu, D. Mondelain, J. Kasparian, E. Salmon, S. Geffroy, C. Favre, V. Boutou and J. Wolf, "Sonographic probing of laser filaments in air," *Applied Optics,* vol. 42, no. 36, p. 7117, 2003.

[129] X. Zeng, X. Mao, S. Mao, S. Wen, R. Greif and R. Russo, "Laser-induced shockwave propagation from ablation in a cavity," *Applied Physics Letters,* vol. 88, p. 061502, 2006.

[130] M. Hauer, D. Funk, T. Lippert and A. Wokaun, "Time resolved study of the laser ablation induced shockwave," *Proceedings of Symposium H on Photonic Processing of Surfaces, Thin Films and Devices, of the E-MRS 2003 Spring Conference*, Vols. 453-454, p. 584–588, 2004.

[131] G. Taylor, "The Formation of a GBlast Wave by a Very Intense Explosion. I. Theoretical Discussion," *Proc. R. Soc. Lond. A,* vol. 201, 1950.

[132] G. Taylor, "The Formation of a Blast Wave by a Very Intense Explosion. II. The Atomic Explosion of 1845," *Proc. R. Soc. Lond. A,* vol. 201, 1950.

[133] M. Richardson and A. Alcock, "Interferometric observation of plasma filaments in a laser produced spark," *Applied Physics Letters,* vol. 18, pp. 357-360, 1971.

[134] R. Fedosejevs, I. Tomov, N. Burnett, G. Enright and M. Richardson, "Self-Steepening of the density profile of a CO2-laser-Producd Plasm," *Physical Review Letters,* vol. 39, no. 15, pp. 932-936, 1977.

[135] S. Raymond and B. Karen, "Optical properties of the," *Appl. Opt.,* vol. 20, pp. 177-184, 1981.

[136] K. Lim, M. Durand, M. Baudelet and M. Richardson, "Transition from linear-to nonlinear-focusing regime in filamentation," *Scientific Reports,* vol. 4, p. 7217, 2014.

[137] J. Noack and A. Vogel, "Laser-induced plasma formation in water at nanosecond to femtosecond time scales: calculation of thresholds, absorption, coefficients, and energy density," *IEEE Journal of Quantum Electronics,* vol. 35, no. 8, p. 1156, 1999.

[138] A. Hansen, R. Geneaux, A. Gunther, A. Kruger and T. Ripken, "Lowered threshold energy for femtosecond laser induced optical breakdown in a water based eye model by aberration correction with adaptive optics," *Biomed Opt. Express.,* vol. 4, no. 6, p. 852, 2013.

[139] R. Salamé, N. Lascoux, E. Salmon, R. Ackermann and J. Kasparian, "Propagation of laser filaments through an extended turbulent region," *Applied Physics Letters,* vol. 91, no. 17, p. 171106, 2007.

[140] R. Ackermann, G. Méjean, J. Kasparian, J. Yu, E. Salmon and J.-P. Wolf, "Laser filaments generated and transmitted in highly turbulent air," *Optics Letters,* vol. 31, no. 1, pp. 86-88, 2006.

[141] G. Mechain, G. Mejean, R. Ackermann, P. Rohwetter, Y. Andre, J. Kasparian, B. Prade, K. Stelmaszczyk, J. Yu, E. Salmon, W. Winn, L. Schlie, A. Mysyrowicz, R. Sauerbrey, L. Woste and J. Wolf, "Propagation of fs TW laser filaments in adverse atmospheric conditions," *Appl. Phys. B,* vol. 80, pp. 785-789, 2005.

[142] A. l'Huillier, L. Lompre, G. Mainfray and C. Manus, "Multiply charged ions induced by multiphoton absorption in rare gases at 0.53 um," *Physical Review A,* vol. 27, no. 5, p. 2503, 1983.

[143] W. Wood, G. Focht and M. Downer, "Tight focusing and blue shifting of millijoule femtosecond pulses from a conical axicon amplifier," *Optics Letters,* vol. 13, no. 11, p. 984, 1988.

[144] M. Mlejnek, E. Wright and J. Moloney, "Femtosecond pulse propagation in argon: A pressure dependence study," *Physical Review E,* vol. 58, no. 4, p. 4903, 1998.

[145] J. Bernhardt, W. Liu, S. Chin and R. Sauerbrey, "Pressure independence of intensity clamping during filamentation: theory and experiment," *Applied Physics B,* vol. 91, pp. 45-48, 2008.

[146] E. Arevalo, "Self-focusing arrest of femtosecond laser pulses in air at different pressures," *Physical Review E,* vol. 74, p. 016602, 2006.

[147] A. Couairon, M. . Franco, G. Mechain, T. Olivier, B. Prade and A. Mysyrowicz, "Femtosecond filamentation in air at low pressures: Part I: Theory and numerical simulations," *Optics Communications,* vol. 259, pp. 265-273, 2006.

[148] G. Mechain, T. Olivier, M. Franco, A. Couairon, B. Prade and A. Mysyrowicz, "Femtosecond filamentation in air at low pressures. Part II: Laboratory experiments," *Optics Communications,* vol. 261, pp. 322-326, 2006.

[149] "atmosphere". Encyclopædia Britannica Online.Encyclopædia Britannica Inc., 2016. Web. 18 Apr. 2016 <http://www.britannica.com/science/atmosphere>.